

Elucidation of the Reaction Mechanisms in Antifluorite-Type $\text{Li}_{5+x}\text{Fe}_{1-x}\text{Co}_x\text{O}_4$ Positive Electrodes for Li-Ion Batteries

Rasmus Vester Thøgersen,^{*[a]} Halvor Høen Hval,^[a] and Helmer Fjellvåg^{*[a]}

The Li-rich antifluorite-type oxides Li_5FeO_4 , $\text{Li}_{5.5}\text{Fe}_{0.5}\text{Co}_{0.5}\text{O}_4$ and Li_6CoO_4 have been investigated as positive electrode materials for Li-ion batteries in a combined *operando* XANES and XRD experiment. All materials show a similar two-step behaviour upon initial charge (termed Stage I and Stage II), and reversibility of subsequent cycling depends upon whether the initial charge cycle is terminated following Stage I or allowed to

proceed through Stage II. By tracking the energetic evolution of the XANES pre-edge feature present in both Fe and Co K-edge spectra, as well as the evolution of X-ray diffractograms during charge and discharge, we correlate the changes in chemical coordination and oxidation states in both species and the structural changes to the electrochemical potential profile, and infer the role of anionic redox processes.

1. Introduction

Pledges to reach net-zero carbon emissions by the middle of this century to curb the most dramatic effects of climate change are being made by an increasing number of governments around the world.^[1,2] An important part of the effort to meet these pledges is the large-scale transition away from a fossil fuel-based society towards one powered by renewable energy.^[3] Electrochemical energy storage plays an integral role in this transition as both stationary energy storage to facilitate integration of intermittent renewable energy sources into the electrical grid, such as solar and wind power,^[4–6] and as the energy source in electrical vehicles (EVs) that are poised to displace a substantial share of the internal combustion engine-based vehicles on the road today.^[7] Lithium-ion batteries (LIBs) are to date dominating the market for EV batteries, most commonly using a positive electrode with either the layered rocksalt material lithium nickel manganese cobalt oxide (NMC), and increasingly the olivine lithium iron phosphate (LFP), as the electrochemically active component. The negative electrode on the other hand consists of graphite or a graphite-silicon composite as the active material.^[7] While there has been a rapid improvement in battery performance since its commercial debut in 1991, owing to both material^[8,9] and engineering^[10] innovations, the energy density of current batteries is still not good enough to replace the internal combustion engine for all

applications, and research continues to pursue ways to further increase it and other important performance metrics.^[11,12]

One obvious route to increase the energy density is to explore materials that have higher specific capacities than the current state-of-the-art active materials. In the positive electrode, both NMC and LFP are limited to exchange 1 Li^+ per transition metal ion, in which the charge is compensated through the oxidation of the transition metal cations. However, over the past decade, Li-rich materials exhibiting anionic redox have been demonstrated, where parts of the charge compensation comes from the partial and reversible oxidation of oxide anions,^[13,14] examples of which include Li_2MnO_3 ,^[15,16] Li_2RuO_3 ^[17,18] and Li_3NbO_4 .^[19] Although still plagued with issues such as capacity loss, voltage decay and sluggish kinetics that pose significant hurdles on the path towards commercial relevance,^[13,14,20] realising a reversible utilisation of the anionic redox mechanism could pave the way towards a significant leap in specific capacities in the positive electrode.

One class of materials that has been shown to exhibit anionic redox contribution is the antifluorite-type compounds, consisting of Li_5FeO_4 ^[21–29] and Li_5FeO_4 ,^[22,30–33] sometimes referred to as hyperlithiated^[34] or super Li-rich compounds.^[35] These materials are particularly interesting for their extremely high Li-contents, which tease the possibility of very high specific capacities. First tested as positive electrode materials in 1999 by Narukawa et al.,^[22] it was later suggested by the same group that these materials exhibit anionic redox following observations that more Li^+ could be extracted than what could be accounted for by redox reactions limited to the transition metal cation.^[23,24] The solid-solution series $\text{Li}_{5+x}\text{Fe}_{1-x}\text{Co}_x\text{O}_4$ was also investigated in the early days,^[24] but did not receive much further attention until recently.^[34] The first papers focused on a relatively shallow cycle depth (for $x \leq 2.0$ in $\text{Li}_{5-x}\text{FeO}_4$ and $\text{Li}_{6-x}\text{CoO}_4$, while Johnson et al. some years later showed that a full 4 Li^+ could be delithiated from Li_5FeO_4 , with two Li^+ each in two distinct voltage plateaus, referred to as Stage I and Stage II in this paper.^[25] The same two-step behaviour during initial charging has also been shown for Li_6CoO_4 ,^[36] and in both cases, charging past Stage I is reported to lead to a large

[a] R. V. Thøgersen, H. H. Hval, H. Fjellvåg

Centre for Materials Science and Nanotechnology, Department of Chemistry, University of Oslo, P.O. Box 1033 Blindern, N-0315 Oslo
E-mail: rasmusvt@kjemi.uio.no
helmerf@kjemi.uio.no

Supporting information for this article is available on the WWW under <https://doi.org/10.1002/batt.202400348>

© 2024 The Authors. *Batteries & Supercaps* published by Wiley-VCH GmbH. This is an open access article under the terms of the Creative Commons Attribution Non-Commercial License, which permits use, distribution and reproduction in any medium, provided the original work is properly cited and is not used for commercial purposes.

irreversible capacity. The poor reversibility following full extraction has also led to much interest in pursuing their potential as sacrificial additives to the positive electrode in LIBs,^[25,33,34,37–40] that could compensate for large first-cycle capacity losses in full cells that use high-capacity active materials in the negative electrode (e.g. Si or SiO_x), as well as a lithium source in lithium-ion capacitors (LICs).^[36,41,42]

In this paper, we investigate the structural and chemical changes upon electrochemical cycling of Li₅FeO₄, Li₆CoO₄ and the intermediate Li_{5.5}Fe_{0.5}Co_{0.5}O₄ by means of *operando* synchrotron experiments in order to better understand the influence of the crystal structure of the starting material and redox active species on the electrochemical properties of the antifluorite-type oxides. In particular, we follow the change in the position of the pre-edge feature of the Fe and Co K-edge spectra using X-ray absorption near-edge spectroscopy (XANES) as a way to keep track of oxidation states during initial charging and subsequent discharge following termination after the initial voltage plateau (Stage I-termination) and after a full initial charge cycle including both voltage plateaus (Stage II-termination). We correlate these changes with X-ray diffraction (XRD) and galvanostatic cycling data. On the basis of this analysis we propose suggestions of reaction pathways and discuss these in light of available literature. Results from additional long-term galvanostatic cycling of coin cells in half-cell configurations are further evaluated to infer changes in redox activity after prolonged cycling.

2. Results and Discussions

Li_{5+x}Fe_{1-x}Co_xO₄ ($x=0.0, 0.5, 1.0$) have been studied electrochemically as positive electrode materials for use in Li-ion batteries. These materials all exhibit an antifluorite-type structure, where Li₅FeO₄ (LFO) assumes the α -variant and Li_{5.5}Fe_{0.5}Co_{0.5}O₄ (LFCO) and Li₆CoO₄ (LCO) assumes the β -variant, nomenclature originally coined by Hoppe and co-workers.^[43,44] The α -variant is described in the Pbca space group, while the β -variant is described in either the tetragonal P4₂/nmc space group (LCO) or the orthorhombic Pmmn space group (LFCO), where the two descriptions differs in the occupancy of a Li-site (a fully occupied 4a site in P4₂/nmc is split into a fully occupied 2a site and a partially vacant 2a site in Pmmn) and a slight orthorhombic distortion ($a \neq b$) in the case of LFCO. Both variants can be considered as a defect 2 × 2 × 2-supercell of Li₂O, where Co²⁺ and Fe³⁺ are charge compensated by either one or two Li⁺-vacancies, respectively. Apart from the β -phase being tetragonal (or near tetragonal), the main difference between the two variants is in the way the transition metal cations and Li⁺-vacancies are distributed within the supercell. In the β -variant, the ordering of cations lead to what can be considered a layered structure, whereas this is not the case for the α -phase. An in-depth presentation of the materials system, including synthesis, structural and physical characterisation, is given earlier by the authors.^[45]

2.1. Initial Formation Cycles

Coin cells of each material in a half-cell configuration were cycled at a specific current of 100 mAg⁻¹ between 1.5 V–4.7 V vs. Li/Li⁺. All materials show similar first charge behaviours, with two distinct plateaus, denoted Stage I and Stage II (Figure 1), consistent with previous reports in the literature.^[25–27,32,38,46] The potential at which these plateaus lie differs between each sample, decreasing with increasing amounts of Co: Stage I is at a potential of 3.6 V vs. Li/Li⁺ for LFO, and decreases to 3.4 V for LFCO and 3.3 V for LCO. Similarly, the Stage II-potential starts at 4.0 V vs. Li/Li⁺ for LFO, decreasing to 3.8 V for LFCO and finally to 3.6 V for LCO. Additionally, the plateaus are more sloped with increasing Fe-content. Lastly, there is a large initial voltage barrier for LFO that is significantly lower in LFCO and almost not present in LCO (Figure S23). The observation of this barrier is consistent with previous reports,^[25,27,39–41] although the exact origin remains unknown.

Stage I corresponds to an extraction of about 1.5, 2.2 and 2.5 electrons per formula unit measured at the midway point between Stage I and Stage II for LFO, LFCO and LCO, respectively. This corresponds to specific capacities of some 260 mAh g⁻¹ for LFO, 370 mAh g⁻¹ for LFCO and 410 mAh g⁻¹ for LCO. The latter is consistent with previous reports,^[32] however, the capacity for LFO is a little lower than the 2 Li⁺ that has been reported before.^[27] This discrepancy could be attributed to a relatively high specific current (e.g. about five times higher than in Ref. [27]) employed in this work, and we indeed show a higher Stage I extraction for LFO during *operando* measurements where a lower specific current of 75 mAh g⁻¹ was used during the initial charge step (Section 2.3).

Stage II corresponds to a further extraction of about 2, 2.8 and 2.5 electrons, corresponding to an additional specific capacity of 350, 470 and 410 mAh g⁻¹. Assuming that all capacity stems from extraction of Li⁺, this corresponds to a total extraction of 3.5, 5 and 5 Li⁺. Note that the transition metal cations would not be able to charge compensate for all Li⁺ extracted. Previous reports show that severe O₂-outgassing

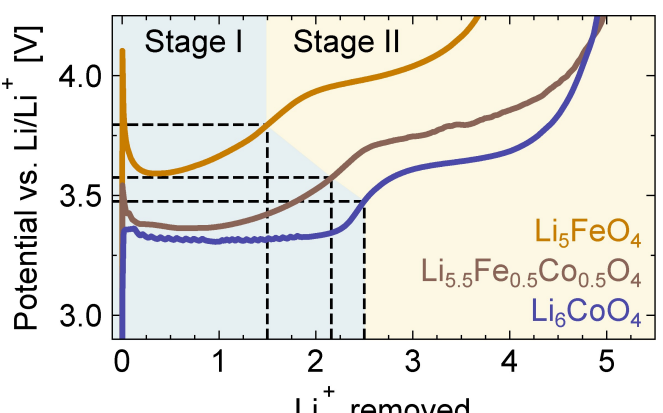


Figure 1. Initial formation charge cycle of Li₅FeO₄, Li_{5.5}Fe_{0.5}Co_{0.5}O₄ and Li₆CoO₄, showing the characteristic two-step behaviour. The two plateaus are denoted Stage I and Stage II, respectively. The potential of each plateau decreases with increasing Co-content. A zoomed-in view of the initial potential barriers is seen in Figure S23.

occurs for both LFO and LCO during Stage II, indicating charge compensation through an irreversible oxidation of oxygen.^[27,32]

2.2. Long-Term Cycling Behaviour

The electrochemical behaviour upon further cycling depends strongly on whether the first charging step is terminated after Stage I or after Stage II (Figure 2). The identification of the two formation stages was in turn used to specify the cutoff voltages, by using the midway point between the average values of each potential step. Termination after Stage I leads to continued reversible cycling for all materials, with an initial increase in capacity in the first 10–25 cycles. LCO, terminated at 3.5 V (Stage I), shows an initial discharge capacity of 200 mAh g⁻¹, which corresponds to about 1.25 Li⁺ being reversibly reinserted, i.e. about half of the first charge capacity (Figure 2, left panel). After an initial increase in capacity to 225 mAh g⁻¹ during the first ten cycles, a rapid capacity decay occurs over the next 100 cycles that flattens out at about 50 mAh g⁻¹, before converging towards a small reversible capacity of 25 mAh g⁻¹ following the next 400 cycles. Termination at 4.7 V (Stage II) leads to an immediate capacity decay, with only 25 mAh g⁻¹ recovered during the first discharge cycle (Figure 2, right panel). This rapidly decreases further, with only a negligible capacity remaining after 50 or more cycles. Cyclic voltammetry (CV) shows a quick deterioration of any electrochemical activity (Figure S28).

LFCO, terminated at 3.6 V (after Stage I), shows an initial discharge capacity of 175 mAh g⁻¹, corresponding to just over 1 Li⁺, i.e. also about half of the first charge capacity. It thereafter exhibits a similar, but less pronounced capacity increase during the next cycles, after which it shows a gradual decrease in capacity for about 150 cycles. At that point there is an onset of more rapid capacity decay over the next 50 cycles, similar to

LCO, that flattens out at about 50 mAh g⁻¹. LFCO also converges to a reversible capacity of around 25 mAh g⁻¹ following a small, gradual capacity fade over the next 300 cycles. Termination at 4.7 V (Stage II) shows a similar behaviour as LCO, although the remnant capacity remains somewhat higher. The same rapid loss of electrochemical activity is confirmed in CV-measurements (Figure S28)

Lastly, LFO, terminated at 3.7 V, shows a much smaller initial capacity of only 75 mAh g⁻¹ (about 0.4 Li⁺), which is about one quarter of the initial charge capacity. Note that a higher initial capacity of 100 mAh g⁻¹ (~0.6 Li⁺) is observed during rate capability testing at 10, which is recoverable after 60 cycles at increasingly higher currents (Figure S30), as well as during the *operando* experiments described below, although this is still considerably lower than the up to 190 mAh g⁻¹ that is previously reported.^[26,27] This is further commented on below. Other previous reports on the reversible discharge capacity for LFO varies, and it is noted that cycling conditions such as cut-off voltages, specific current and temperature varies considerably. There is a small increase in the capacity over the first 25 cycles where it stabilises for another 75 cycles. The steep decline in capacity that was observed for LCO and LFCO is not present for LFO. Instead, a gradual capacity fade for the next 400 cycles is observed, before it also converges to about 25 mAh g⁻¹ similar to both LCO and LFCO. Stage II-termination for LFO leads to a very different behaviour than LCO and LFCO. An initial discharge capacity of 100 mAh g⁻¹ is achieved, followed by a gradual decrease towards 50 mAh g⁻¹ over the next 400 cycles, at which point the cell failed. CV-measurements show a significant difference between continued electrochemical activity following Stage I and Stage II termination in the first 20 cycles (Figure S28).

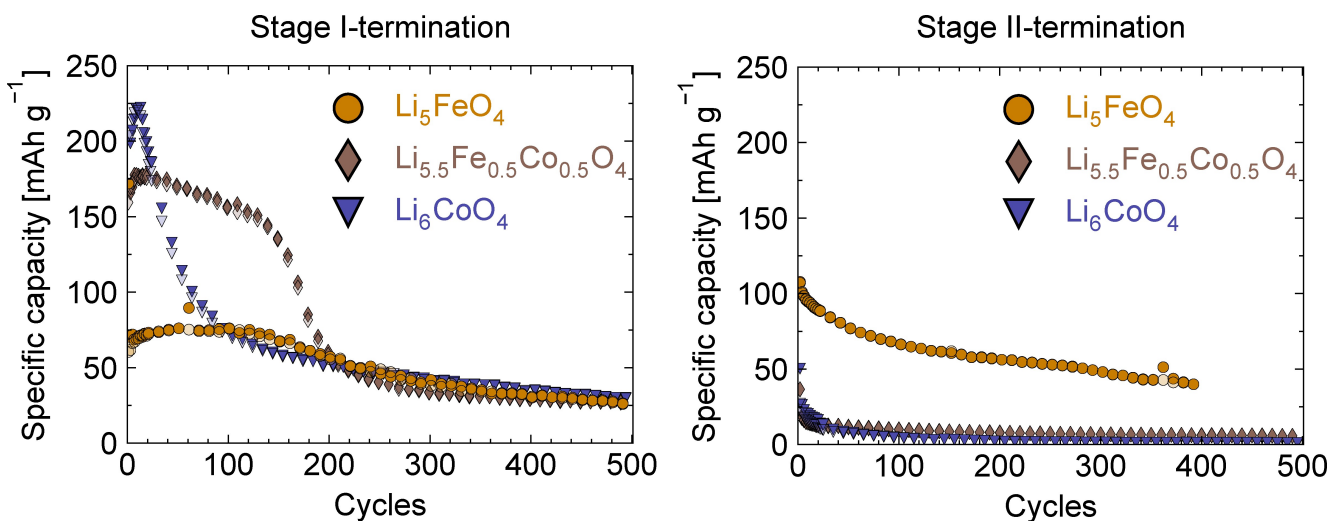


Figure 2. Galvanostatic cycling for half-cells of Li₅FeO₄, Li_{5.5}Fe_{0.5}Co_{0.5}O₄ and Li₆CoO₄ following (Left panels) Stage I-termination and (Right panels) Stage II-termination. All cells are cycled at 100 mA g⁻¹. The Li₅FeO₄-cell cycled following Stage II-termination failed after about 400 cycles. For the first 25 cycles, every second data point is plotted. After this, every tenth data point is plotted for legibility. See supplementary information (Figures S24 and S25) for complete cycle data, including Coulombic efficiency.

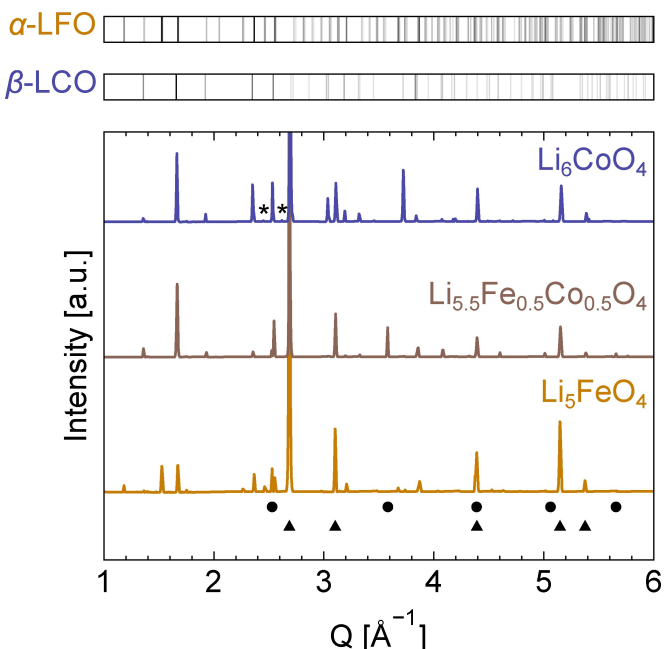


Figure 3. Initial X-ray diffractograms of $\text{Li}_{5+x}\text{Fe}_{1-x}\text{Co}_3\text{O}_4$ in assembled *operando* cells, prior to start of first cycle. Peaks associated with the Li-metal disks (negative electrode) are marked with circles (•), while peaks associated with the aluminium current collector are marked with triangles (▲). Li_2O_2 impurity peaks in LCO are marked with an asterisk (*).

2.3. Operando Measurements

In order to obtain insights into structural and electronic changes during the initial charge and cycling after Stage I- or Stage II-termination, *operando* XANES- and XRD-measurements were carried out with synchrotron radiation for all materials under investigation. After being assembled in *operando* cells, the uncycled materials were initially confirmed to retain their pristine α - and β -structures (Figure 3) with tetrahedrally coordinated (T_d) Fe^{3+} - and Co^{2+} -cations. Some signs of Li_2O_2 are visible in the diffractogram for LCO (e.g. $Q=2.3$, 2.45 and 2.8 \AA^{-1}), but as elaborated on below, this is assumed to be present on the negative electrode without participating in the electrochemical reactions. There are some differences in the relative intensities of the LFCO and LCO Bragg peaks in comparison with diffractograms from previous static capillary measurements of the pristine materials measured in transmission mode.^[45] As we see no indications of any new phases that could arise from any adverse reactions (such as with H_2O or CO_2), we judge these discrepancies to be likely attributable to preferred orientation effects owing to the non-ideal experimental conditions imposed by the *operando* cell. The tetrahedral chemical environments are confirmed by XANES Fe and Co K-edge signature spectral shapes (Figure 4, thick dark spectra). The characteristic A1–A3 main peaks originate from $1s \rightarrow 4p$ dipole transitions, while the shoulder peak B originates from a two-step process where a $1s \rightarrow 4p$ transition is followed by a charge transfer from $\text{O} 2p$ to $M 3d$ ($M=\text{Fe}, \text{Co}$), leading to a final state of $1s 1\zeta 3d^{n+1} \underline{L} 4p$ where ζ is a core-hole and \underline{L} is a ligand.

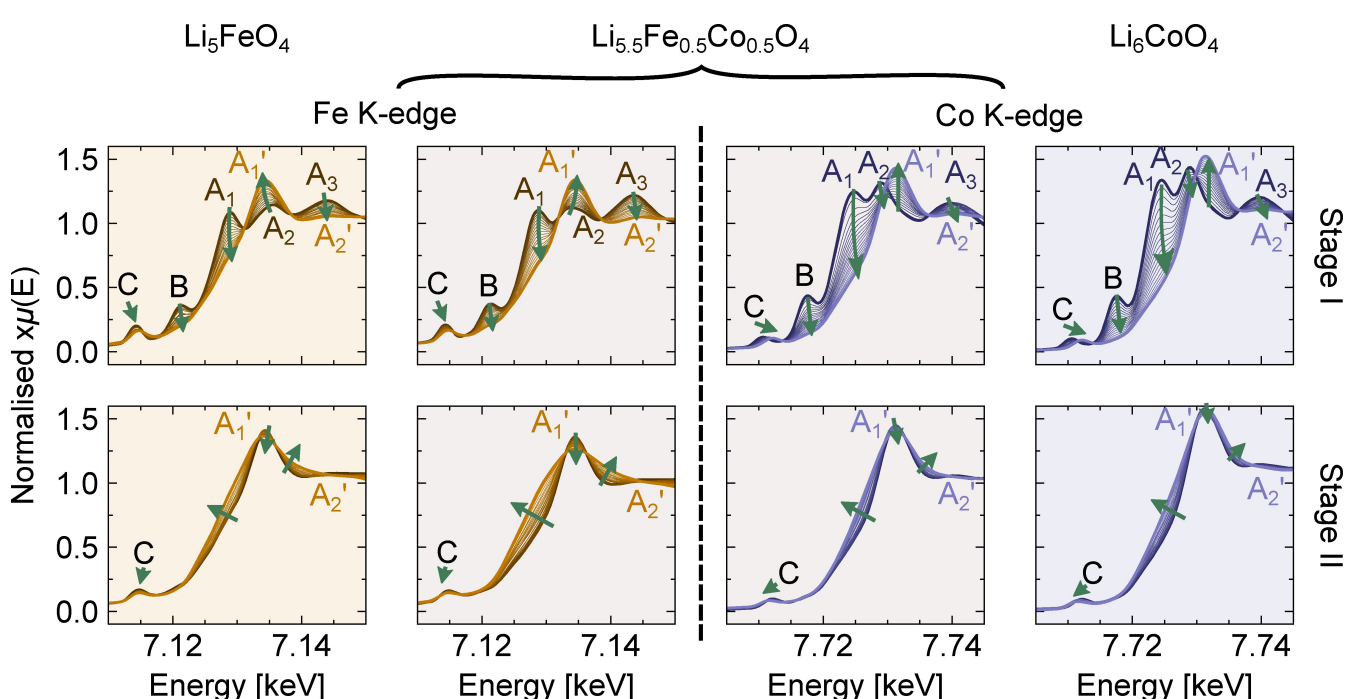


Figure 4. XANES-spectra of the Fe and Co K-edges during (Top row) Stage I-charging and (Bottom row) Stage II-charging. Arrows indicate direction of change with cycling. The same kind of changes are observed for both edges, with a transition from a signature T_d -symmetry before start to O_h -symmetry after Stage I, with a concurrent shift in both edge and pre-edge positions towards higher energies, indicating oxidative behaviour. No further changes in coordination is observed during Stage II, however a lowering of edge and pre-edge positions occurs in this region, indicative of reductive behaviour. Larger versions for each charge and discharge step, including a zoomed-in view of the pre-edge peak C, are given in the supplementary information.

hole.^[26] This transition is also observed in e.g. $\gamma\text{-Fe:LiAlO}_2$, believed to be strengthened from a covalent mixing of Fe $4p$ - and O $2p$ -orbitals. The pre-edge feature C originates from the $1s \rightarrow 3d$ -transition, which is dipole allowed in T_d -symmetry due to hybridisation of $3d$ - and $4p$ -orbitals, both of t_2 -symmetry, allowing transfer to the p -character of the orbitals ($\Delta l = 1$).^[47] This $1s \rightarrow 3d$ -transition is quadrupole allowed ($\Delta l = 2$), but such a transition has a much weaker intensity.^[48] The mixing of $4p$ - and $3d$ -orbitals is symmetry-forbidden in octahedral symmetry (O_h), hence such a pre-edge feature is predicted to be weaker in the latter case.

During charging at Stage I, all materials show a continuous change in the XANES spectral shape (Figure 4). The changes are immediate upon start of the charge cycle. The main peaks A1–A3 transform to A1' and A2', while the shoulder peak B diminishes greatly and becomes only barely visible in the rising edge after Stage I. The pre-edge peak C also diminishes in intensity, in particular in the Fe K-edge spectra. This is all indicative of a continuous increase in the mass fraction of transition metal cations with O_h vs. T_d symmetry, and is in agreement with previous reports.^[26,27,32] There is also an energy shift of both the main absorption edge and the pre-edge feature, and the centroid position of the pre-edge feature C is further used to keep track of changes in oxidation states during the cycling, as this is known to strongly correlate with valence.^[48,49] With increasing oxidation state, the pre-edge feature will shift towards higher energies.

2.3.1. Li_6CoO_4

Stage I-Termination | LCO

For LCO there is a continuous, linear increase in the pre-edge energy for the first two electrons per formula unit corresponding to an oxidation of $\text{Co}^{2+} \rightarrow \text{Co}^{4+}$, before it flattens out for the remaining 0.4 electrons (Figure 5). The total energy shift for the C pre-edge feature after transfer of two electrons is 1.5 eV. The charging plateau is completely flat in this region and the XANES-spectra show several isosbestic points, both being indicative of a two-phase reaction. XRD patterns show that the main peaks corresponding to the β -phase remain visible for extraction corresponding to the first electron, but gradually diminish in intensity and vanish halfway through Stage I. During the first half, there are no signs that the β -phase peaks are shifting in position, which would be expected if Li^+ was directly delithiated from the antifluorite crystal structure, as that would lead to a change in lattice parameters of the crystal structure. About halfway through Stage I, a new, quite broad diffraction peak becomes visible at $Q=1.3 \text{ \AA}^{-1}$ (Figure 6). This peak could be attributed to the most intense (00l)-peak of a layered rocksalt-phase, such as LiCoO_2 or Li_2CoO_3 , although it must be noted that no other peaks matching any of these phases are observed, and further studies are required to confidently confirm and refine this phase. At the same time, two other peaks appear, one at $Q=2.35 \text{ \AA}^{-1}$ and one at $Q=3.8 \text{ \AA}^{-1}$, both at slightly higher angles than two of the diminishing antifluorite peaks. These new peaks match well with the main (111) and (220) diffraction peaks of Li_2O . All new peaks increase in intensity until the end of the charge cycle. The Li_2O_2 -peaks noted above remain unchanged throughout the entire process,

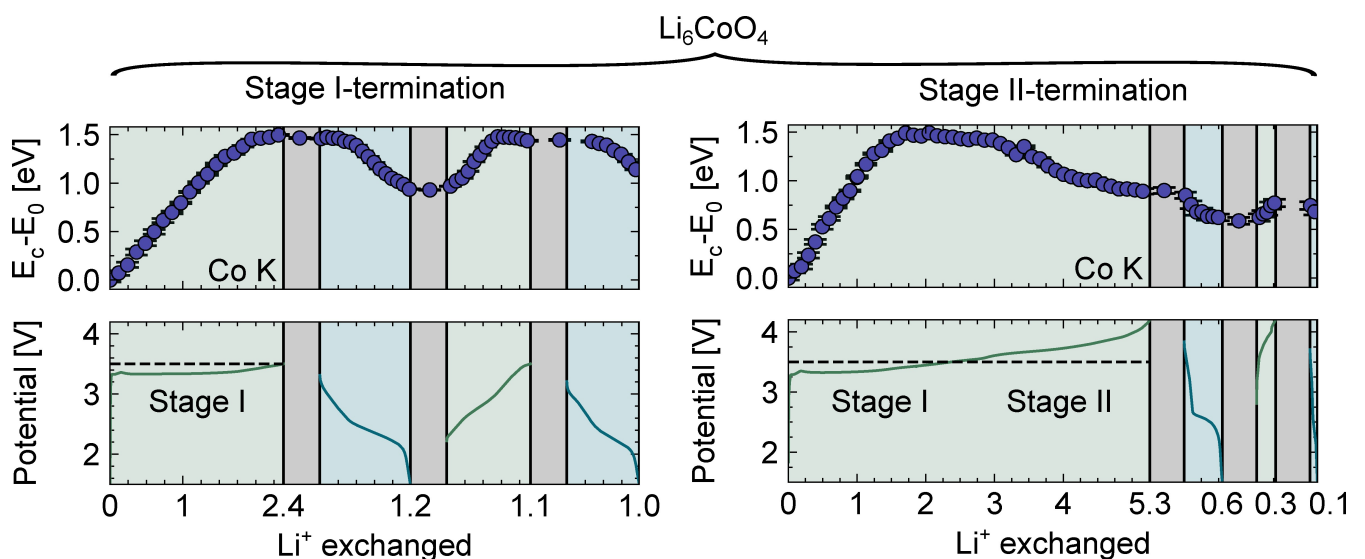


Figure 5. Combined galvanostatic cycling (potential vs. Li/Li^+) and relative position of the XANES Co K pre-edge peak as a function of Li^+ exchanged in Li_6CoO_4 following (Left panels) Stage I-termination and subsequent cycling and (Right panels) Stage II-termination and subsequent cycling. Charge (green) and discharge steps (blue) are separated by a resting step (gray) of 15 minutes to ensure collection of XANES-spectra while resting. Position of the pre-edge peak is given relative to the initial value before cycling. Counting of exchanged Li^+ is reset after each resting step, where the zero labels have been omitted for legibility.

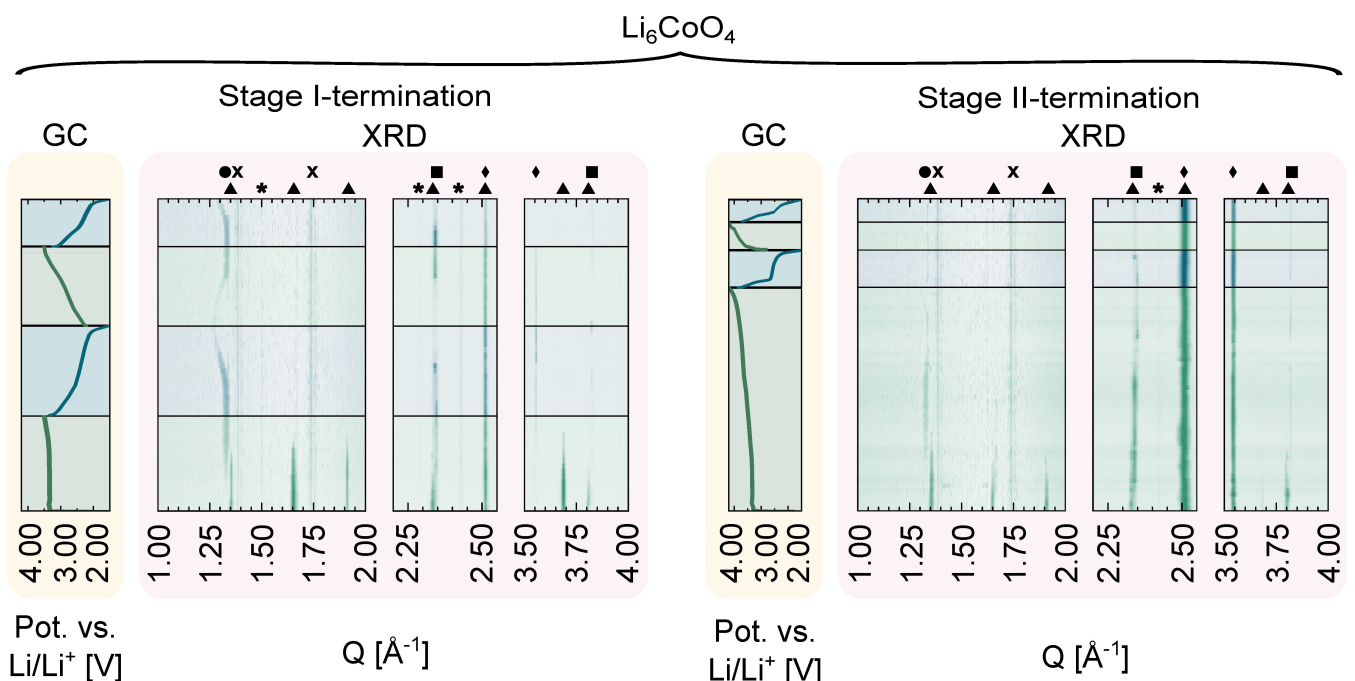


Figure 6. *Operando* X-ray diffractograms (XRD) of selected values of Q for Li_6CoO_4 and corresponding potential curves (GC) during (Left panels) Stage I-termination and subsequent cycling and (Right panels) Stage II-termination and subsequent cycling. Runs from bottom to top, with charge steps in green and discharge steps in blue. Intensities plotted as $\log I$ for enhanced contrast. Symbols above indicate peak positions of LCO (▲), Li_2CoO_3 (●) and Li_2O (■), Li_2O_2 (*). Artefacts following background subtraction are also marked (x). Full diffractograms are given in Figures S21 and S22.

and is thus assumed to be present on the negative electrode without participating in the electrochemical reactions.

Based on this, we propose that the transfer of the first two electrons (of a total of 2.4 e^- in Stage I) follows the reaction:



This behaviour differs from what was proposed by Kobayashi et al. in the case of ball-milled LCO, although having several similarities.^[32] In their case, ball-milling of pristine β -LCO triggered an order-disorder transition to a disordered cubic antifluorite-phase, a transition that is also observed upon heating, and denoted the ε -phase by the present authors.^[45] In the ε -phase, there is a complete cation-disorder over the tetrahedral sites. The initial charge curve of ε -LCO show two distinct plateaus rather than one during Stage I-charging, indicating that there are two distinct electrochemical processes ongoing. Kobayashi et al. proposed an initial topotactic delithiation of the antifluorite phase, in line with the first plateau they observed. Jun et al. suggested a similar topotactic reaction for β -LCO for the first half of the Stage I-plateau.^[33] However, our XANES-data show a continuous change in coordination throughout the entire plateau, indicating that the migration from $T_d \rightarrow O_h$ starts already for the first electron extracted. Furthermore, there are no visible shifts in the Bragg peak position associated with the antifluorite phase during this reaction that could indicate changes in lattice parameters. We note that no shifts are visible in the data presented by Jun et al.

either. We hence conclude that the topotactic delithiation reaction does not occur within a cation-ordered β -LCO, and that the entire two electron region is indeed a two-phase reaction described entirely by Eq. (1).

Furthermore, Kobayashi et al. reported a disordered variant of Li_2CoO_3 as product. We do not observe any characteristic diffraction peaks for a disordered rocksalt phase, but instead observe a peak that seems to match the characteristic (00)-peak of a layered rocksalt variant. We suggest that what is observed is the Li-excess layered variant, similar to what has been reported for Li_2MnO_3 ^[15,16] and Li_2RuO_3 ^[17] with $C2/m$ space group symmetry, in which the excess Li is situated in the TM-cation layer in a honeycomb pattern. The structural differences probably have roots in the structures of the starting materials. In β -LCO, the ordering of the Co-ions can already be considered to be layered (Figure 7, left), with alternating layers of (Co₆Li) and Li-only. The most facile collective migration from $T_d \rightarrow O_h$ will result in a layered structure (Figure 7, right). This would not be the case if the starting material were disordered. The broadness of the (00l) peak and absence of any other peaks indicate that the TM-cation layer is not perfectly ordered, but shows some intralayer disorder. The layered Li_2CoO_3 -phase was also suggested by Jun et al. in their thermodynamic treatment of possible reaction pathways, although they concluded that this occurred together with the formation of Li_2O_2 .^[33] As we instead observe appearance of diffraction peaks of Li_2O , and a continuous and linear shift in the pre-edge centroid position throughout the whole 2 electron reaction, we conclude that this reaction must occur according to Eq. (1) instead, where all

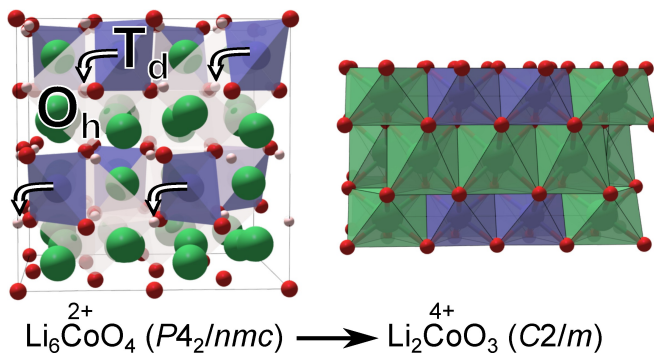


Figure 7. The proposed transition of Li_6CoO_4 to Li_2CoO_3 during Stage I-charging. Tetrahedrally coordinated Co and Li (T_d) migrate collectively to octahedral sites upon removal of Li^+ .

the redox activity can be attributed to the $\text{Co}^{2+}/\text{Co}^{4+}$ redox couple.

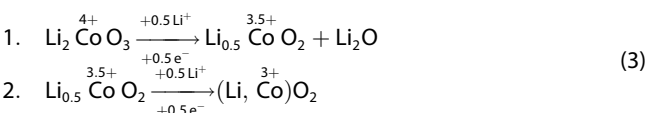
Upon further charging, the energy position of the pre-edge feature flattens out, showing only minor changes. This indicates that the charge compensation is no longer attributable to Co. This is proposed to follow from the reaction:



for parts of the newly formed Li_2O . This is in line with what was reported for ε -LCO, where XANES data for the O K-edge provided evidence for the existence of peroxide species.^[32] This should be independent of the initial structural state of the active material, as this reaction only involves newly formed Li_2O . The formation of Li_2O_2 is not directly observed in the XRD-data, as any new peaks would be weak and obscured by the existing Li_2O_2 -peaks stemming from the negative electrode. In this region, there is an increase in potential, indicating the end of the two-phase reaction. The process continues for 0.4 electrons per formula unit before reaching the specified cut-off potential of 3.5 V vs. Li/Li⁺.

Upon discharge, this process is reversed, as evident from the energy position of the pre-edge feature, which does not move for the reinsertion of the first 0.4 Li^+ . This corresponds well to the first slope in the discharge curve. There is no visible change in the diffractograms during this plateau. After this slope, the pre-edge feature starts to decrease in energy, indicating that Co is again the redox active species, but the centroid position of the pre-edge feature never reaches the same position as for the starting material, but rather stops approximately 0.9 eV above the pristine state. This corresponds well to its position after extraction of 1 Li^+ during the first charge cycle, and thus to a formal oxidation state of Co^{3+} . The difference in magnitude of the energy shift between the $\text{Co}^{2+}/\text{Co}^{3+}$ and the $\text{Co}^{3+}/\text{Co}^{4+}$ redox couples could be attributed to the increase in metal-ligand bond covalency at higher oxidation states, where ligand holes are formed on O 2p that decreases the charge on Co. This is described in further detail for the case of LFO below.

At the same time the (00l) diffraction peak moves towards lower angles (i.e. higher interlayer spacings), while it diminishes in intensity. This might at first seem counter-intuitive, as a shift towards higher interlayer spacings suggests removal of Li^+ from the layered structure due to the increased electrostatic repulsion between the metal layers. But this happens at the same time as Li^+ is inserted into the structure during discharge. Hence, we propose the following two-step pathway as a possible explanation:

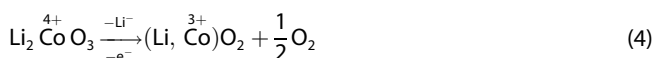


Here $(\text{Li}, \text{Co})\text{O}_2$ is assumed to take a disordered rocksalt structure. However, we note that we see no evidence of such a phase in the diffractograms, which could possibly be due to an overlap of the Bragg peaks of the resulting phase with the strong peaks from the Al current collector. Alternatively, the new phase could be poorly crystallised. This process is reversible, as evident by the reemergence of the (00l)-peak upon a second charge cycle, including a shift towards higher Q, that would indicate that Li^+ re-enters the structure and the intralayer spacing decreases again. The change in oxidation state, as seen from the pre-edge position, also shows a full return to Co^{4+} before flattening out and thereby again indicating oxidation of Li_2O according to Eq. (2). A slight decrease in capacity is observed between the first and second discharge cycle, which is in line with observations in long-term cycling (Figure 2, left panel), where the discharge capacity first decreases in the second and third cycles, before showing a gradual increase until the tenth discharge cycle. In this process, the plateau associated with oxidation of Li_2O becomes more pronounced as a plateau (Figure S26). Upon the rapid degradation that follows for the next 90 cycles, there is a gradual shortening of both the plateau associated with Li_2O -oxidation as well as with the $\text{Co}^{3+}/\text{Co}^{4+}$ redox couple.

Stage II-Termination | LCO

When extending the initial charge into the Stage II region, a seemingly flat plateau of the pre-edge position (Figure 5, right) remains for the extraction of about 1 electron, which corresponds to the length of the transition between the two potential plateaus. The one electron could correspond well with a completion of the reaction in Eq. (2), however, previous differential electrochemical mass spectroscopy (DEMS)-studies have shown the onset of O_2 -outgassing at the midway point between the two plateaus.^[32,33] This suggests instead that further Li^+ is extracted from the newly formed Li_2O_2 which in turn is oxidised to O_2 . This is consistent with XRD-data showing the persistence of the newly formed Li_2O_2 -peaks. After this point ($x > 3$) however, there is a very clear decrease in the centroid position, ending at the same position as after Stage I-discharge, namely 0.9 eV above the pristine state. This indicates the reduction of Co back to Co^{3+} . This occurs simultaneously as the

peak intensity of Li_2CoO_3 diminishes, indicating a structural transition to a disordered state, similarly to what happens in step 2 of Eq. (3), although starting from Li_2CoO_3 instead. There are no signs of change of the intralayer spacings during this process. As Li^+ at this Stage is still extracted from the positive electrode, there must be a charge compensation for both the Li^+ -removal and the reduction of Co^{4+} to Co^{3+} . The reaction:



can account for the extraction of one additional electron, although this indicates a higher O_2 -release per electron than what is suggested by previous *in situ* DEMS-experiments, which instead suggests that O_2 -release slows down after the initial 1 electron reaction described above.^[32,33] The last electron could additionally be attributed to the final decomposition of the remaining Li_2O , and would likely be the major contributor towards the end of the charge process as the shift of the pre-edge position slows down. However, diffraction peaks attributable to Li_2O remains at the end of Stage II-charging, ruling out a complete oxidation of previously formed Li_2O . It cannot be ruled out that at least some part of the last 2.3 e⁻ could involve irreversible reactions of unstable peroxide-like species with the electrolyte. DEMS-measurements by Jun et al. showed evolution of CO_2 towards the end of the initial charge step, indicating breakdown of the carbonaceous electrolyte, but we would like to point out the unusual charge behaviour of Stage II during this experiment in which a third plateau appears, not otherwise observed. This behaviour indicates that the onset of CO_2 -evolution happens following some side-reaction owing to the experimental setup, and is not inherent of the active material, which seems to have reached completion of Stage II prior to

the majority of the reported CO_2 -outgassing. However, it is not clear whether the onset of outgassing that Jun et al. reports occurs prior to or after completion of Stage II. Additional experiments to fully understand the mechanisms towards the end of Stage II are warranted.

Although some capacity is still observed for the first discharge, most of this is attributed to a process that does not involve Co, and is not recovered in the subsequent charge cycle, (Figure 5). This could be an irreversible side reaction that is enabled after the full degradation following Stage II. There is a slight reduction of Co during discharge in which the centroid position of the pre-edge feature shifts down in energy by about 0.3 eV, indicating the reduction of some Co^{3+} to Co^{2+} , and it is not fully oxidised back to Co^{3+} after the second charge where a very small charge capacity of 0.3 electrons is observed. There is an even smaller capacity upon the second discharge (0.1 electrons). This rapid capacity fading corresponds well to the behaviour seen for long-term cycling (Figure 2).

2.3.2. Li_5FeO_4

Stage I-Termination | LFO

About 1.8 electrons were extracted from LFO during Stage I (Figure 8), which is higher than what was observed in the coin cell experiment (1.5 electrons). This difference can be attributed to the lower specific current of 75 mA g⁻¹ used during the initial formation in the *operando* cell vs. 100 mA g⁻¹ used in the coin cells. At the end of Stage I, there are remnants of the XANES shoulder peak B (Figure 4, top left panel), while some of the antifluorite peaks in the diffractograms remain (Figure 9), which disappear upon further cycling into Stage II. This indicates that

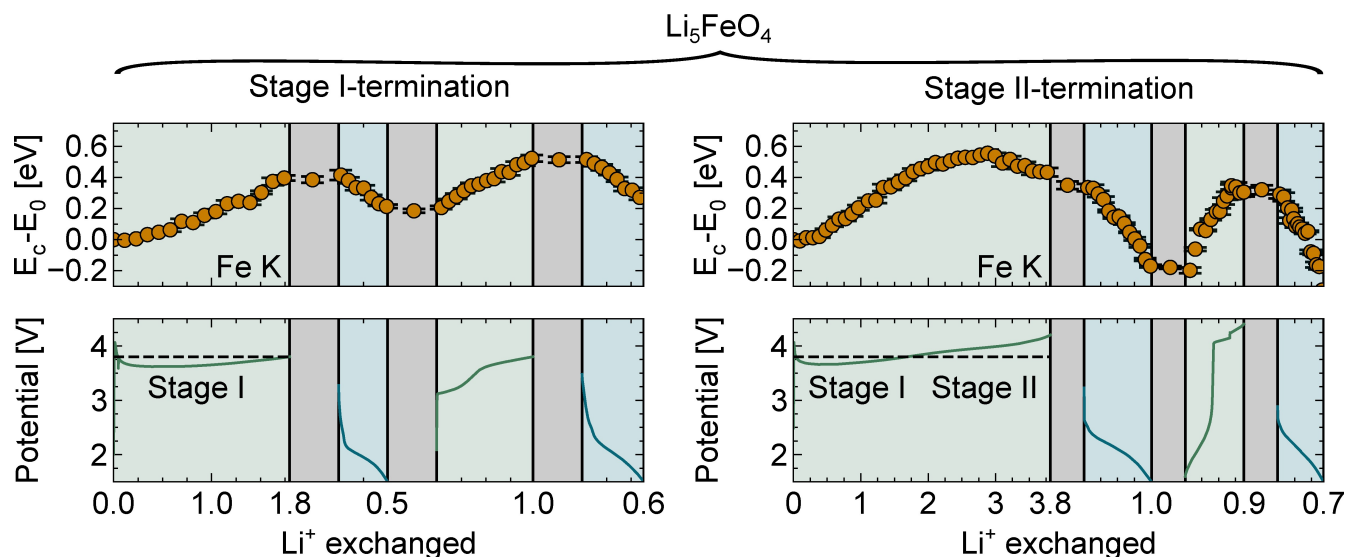


Figure 8. Combined galvanostatic cycling (potential vs. Li/Li^+) and relative position of the XANES Fe K pre-edge peak as a function of Li^+ exchanged in Li_5FeO_4 following (Left panels) Stage I-termination and subsequent cycling and (Right panels) Stage II-termination and subsequent cycling. Charge (green) and discharge steps (blue) are separated by a resting step (gray) of 15 minutes to ensure collection of XANES-spectra while resting. Position of the pre-edge peak is given relative to the initial value before cycling. Counting of exchanged Li^+ is reset after each resting step, where the zero labels have been omitted for legibility.

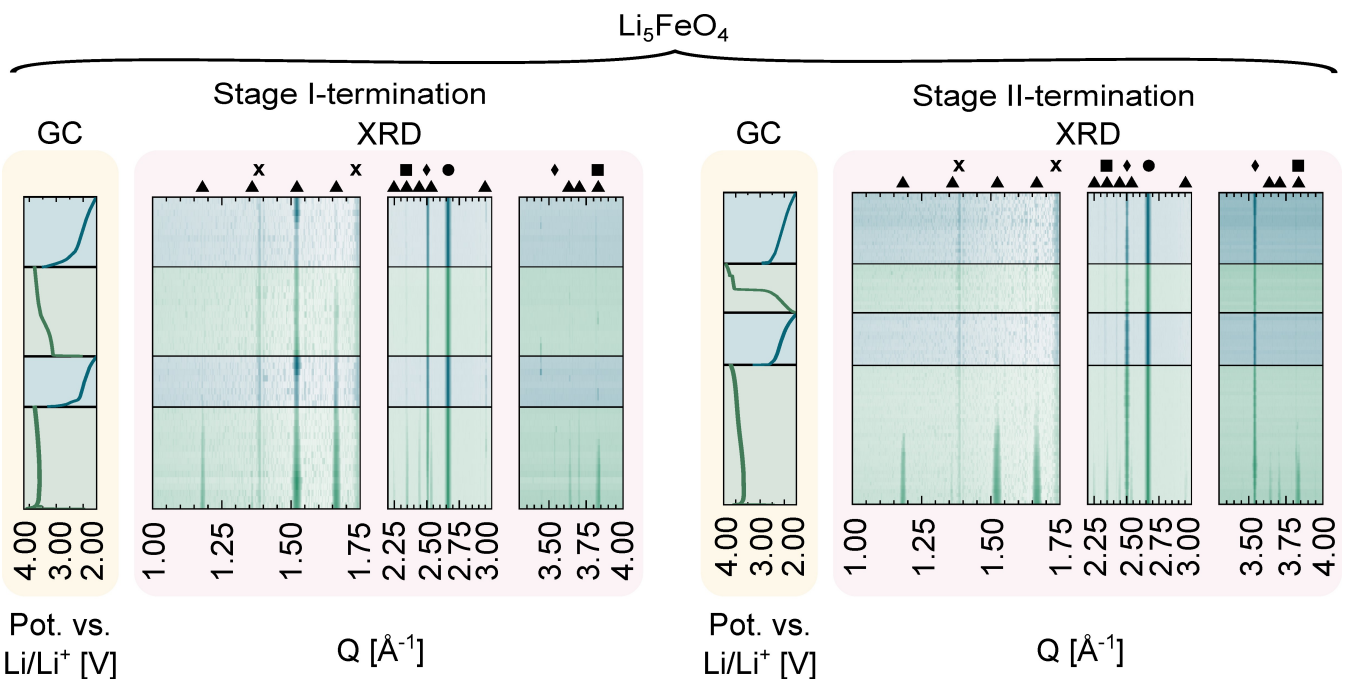


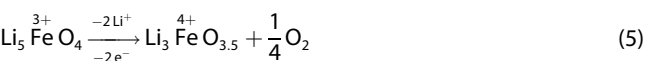
Figure 9. *Operando* X-ray diffractograms (XRD) of selected values of Q for Li_5FeO_4 and corresponding potential curves (GC) during (Left panels) Stage I-termination and subsequent cycling and (Right panels) Stage II-termination and subsequent cycling. Runs from bottom to top, with charge steps in green and discharge steps in blue. Intensities plotted as $\log I$ for enhanced contrast. Symbols above indicate peak positions of LFO (\blacktriangle), Li_2O (\blacksquare), the aluminium current collector (\bullet) and the Li-metal negative electrode (\blacklozenge). Artefacts following background subtraction are also marked (x). Full diffractograms are given in Figures S17 and S18.

the initial charge process is not entirely completed at 3.7 V. In the following, we assume that two electrons could be extracted during Stage I.

The set of *operando* XANES-spectra show several isosbestic points, which along with the flat potential plateau in the GC curves indicates a two-phase process for extraction of two electrons, similar to LCO. There is a continuous, linear increase in energy of the centroid position of the Fe pre-edge feature C throughout the entire charge step, which ends at around 0.4 eV above the pristine state after Stage I (Figure 8, left panel). As noted above, there is evidence that the full transformation of the pristine antifluorite phase is not completed at this point, and the pre-edge feature shifts another 0.1 eV to a maximum of 0.5 eV vs. the pristine state following the second charge cycle. This is the same maximum value as is obtained after a full 2 Li^+ has been extracted when extending the initial charge into Stage II (Figure 8, right panel). This indicates that around 0.2 Fe remains in a trivalent state at the end of Stage I, which accounts for the additional 0.2 Li^+ assumed to be extractable in Stage I. Zhan et al. correlates the shift in edge energy to an average valence of $\text{Fe}^{3.5+}$,^[27] however, the magnitude of the shift of the centroid position seems to be similar to previous reports of shifts attributed to Fe^{3+} to Fe^{4+} in $\text{SrFeO}_{3-\delta}$,^[50] and $\text{La}_{1-x}\text{Sr}_x\text{FeO}_4$,^[51] although quantification of the centroid position is lacking in these cases making a direct comparison difficult. The much smaller shift in the pre-edge position for $\text{Fe}^{3+} \rightarrow \text{Fe}^{4+}$ with respect to $\text{Fe}^{2+} \rightarrow \text{Fe}^{3+}$ (~1.4 eV)^[49] has previously been attributed to a much higher degree of covalency of the Fe–O-bond as the formal charge of Fe increases, thus making the

contribution of O 2p-bands more important.^[50] This leads to a strong mixture of $3d^4$ -states and $3d^5L$ -states, where L is a ligand-hole in the O 2p-orbitals, which in turn leads to a lower effective charge on Fe.^[52,53] The high degree of covalency is reflected in the calculated electronic density of states of LFO that shows a large degree of mixed Fe/O-character for the $(\text{Fe}^{3+}\text{O}_4)^{5-}$ -ions (similar to what is also seen in calculations of the related Na_5FeO_4),^[54] visualised by the computed Fukui function that shows electronic states of high O 2p-character at the Fermi-level.^[45]

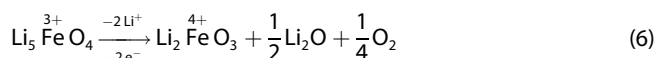
This $\text{Fe}^{3+} \rightarrow \text{Fe}^{4+}$ oxidation process, which could be described as a simultaneous cationic/anionic redox process due to the strong admixture of O 2p-states, can only account for one of the two electrons required for charge compensation. Previous DEMS-studies by Zhan et al. showed a small gas release already during Stage I, and they proposed a mechanism where two Li^+ is extracted along with 0.25 O_2 disassociating irreversibly from the lattice, where the latter process accounts for the second electron.^[27] They describe the process as:



in which the formal charge of Fe is 4+, but the strong covalent character of the Fe–O-bonds according to the discussion above should be noted. Structurally, this leads to formation of a disordered rock salt phase (DRP), although we note that such a DRP-phase is not observed in our diffractograms (Figure 9). This lack of observation could be because the expected broad

diffraction peaks from the DRP described by Zhan *et al.* ($a=4.064 \text{ \AA}$) has significant overlap with the strong diffraction peaks from the aluminium current collector ($a=4.0494 \text{ \AA}$,^[55] and as such is not discernible in our data. The suggested DRP-structure that results from the removal of Li^+ and irreversible loss of oxygen from the structure that yields randomly distributed oxygen vacancies, has a resulting oxygen vacancy concentration of 12.5%, which is indeed a very high value. We envisage that such a structure will not be stable, and rather undergo a reconstruction, with all oxygen sites filled, and a likewise increased amount of lithium and iron in the tetrahedral or octahedral voids. Assuming Eq. (5) to be correct, the renormalised composition of the DRP material would then be $\text{Li}_{3.43}\text{Fe}_{1.14}\text{O}_4$, requiring the filling of 0.57 tetradral voids per formula unit. Since we do not observe any reappearance of the B shoulder peak in the XANES-spectra (Figure 4, top left panel), we conclude that if this is the case, no Fe-cations reoccupy any tetrahedral voids. This implies that 0.57 Li^+ must occupy tetrahedral voids, probably with short range correlation with Li^+ at octahedral sites.

However, while the diffraction peaks associated with α -LFO diminishes in intensity during charge, some of the peaks have not fully disappeared by the end of Stage I, and towards the end of the first discharge, the peaks from the set of planes corresponding to {201} in the ideal cubic antifluorite ($Q=1.5 \text{ \AA}^{-1}$) again increase in intensity, although seemingly independent of the other peaks. Following the next charge step, this peak is one of the only peaks of α -LFO that remains clearly visible, again increasing in intensity towards the end of the second discharge step. The other peak that remains visible throughout is seen at $Q=2.9 \text{ \AA}^{-1}$ which can be indexed to the {313}-set of planes, although this peak changes in intensity throughout all the cycling steps in an apparent unsystematic manner. The increase in intensity of the {201}-peak occurs simultaneous to the reemergence of a peak that could be indexed to the {431}-set of planes in α -LFO at $Q=3.45 \text{ \AA}^{-1}$. The significance of these peaks are not fully understood, and it is not ruled out that they belong to another phase entirely. The main Li_2O -peaks are also observed at $Q=2.35 \text{ \AA}^{-1}$ (111) and 3.8 \AA^{-1} (220), appearing towards the end of Stage I, indicating that some Li_2O is formed alongside the O_2 -outgassing, challenging the assumption made by the reaction in Eq. (5). Instead, we propose another possibility of what happens during Stage I that accounts for the formation of Li_2O , which could be described as:



The resulting product is similar to what was seen for LCO in Eq. (1). While Li_2CoO_3 was suggested to have a layered structure based on the emergence of a characteristic diffraction peak, there are no similar signs that Li_2FeO_3 is layered. The difference between the pristine antifluorite α - and β -phases lies mainly in the way the transition metal cations are distributed in the unit cell, and the same initial layered structure in β -LCO (Figure 7) is not present in α -LFO.^[45] Thus, the most facile collective movement would instead result in a rocksalt structure with Li^+ and

Fe^{4+} distributed throughout all octahedral sites, similar to what Koboyashi *et al.* proposed for their ball-milled disordered ϵ -LCO.^[32] Such a structure would indeed have overlapping peaks with the oxygen deficient variant that Zhan *et al.* proposed.

The peak intensities of Li_2O seemingly remain constant throughout the next discharge process, thus showing no apparent signs of anionic redox participation as was observed for LCO, although the intensities are too weak to conclude firmly.

In the discharge following Stage I-termination, only 0.5 Li^+ is reinserted into the positive electrode. This is approximately half of what Zhan *et al.* (1.1 Li^+)^[27] and Okumura (0.9 Li^+)^[26] reported. In the work by Zhan *et al.*, they show a two step discharge curve following Stage I-termination, one between 3.0–2.0 V corresponding to half an electron, while the second slope between 2.0–1.0 V corresponds to the remaining 0.6 electrons. They attribute the entire reaction to a combined redox activity from the O^{2-}/O^- and $\text{Fe}^{3+}/\text{Fe}^{4+}$ redox couples. Here, the first slope is seen to be severely shortened (Figure 8, left), corresponding only to slightly less than 0.1 Li^+ . This is the main source of the discrepancy between the reversible capacities. The second slope proceeds for half an electron until reaching the lower cut-off voltage of 1.5 V and is in good agreement with previous results, despite a higher cut-off voltage (0.5 V higher than in Zhan *et al.*).^[27] The absence of the first plateau could simply be attributed to the incomplete reaction during Stage I, but as that would only account for 0.2 electrons, it is also likely that the first plateau is related to a kinetically sluggish process that becomes restricted by the relatively high specific current employed. The same shortening of the first plateau is also observed in the first discharge in coin cells cycled at 100 mA g^{-1} . During the discharge, the centroid position of the pre-edge feature shifts down in energy, in what appears to be a strictly linear fashion, but stops only about halfway towards the initial value, some 0.2 eV above it, suggesting that a full reduction of Fe^{4+} back to Fe^{3+} does not occur, but rather a partial reduction to an average oxidation state of approximately $\text{Fe}^{3.5+}$.

Upon the second charge step, the centroid position of the pre-edge feature again increases in energy, this time to its maximum value of 0.5 eV above the pristine state. The potential curve shows a gradually increasing plateau at the same potential as Stage I, after the initial 0.5 Li^+ had been reextracted, and it is during this plateau that the pre-edge position moves the last 0.1 eV. This indicates the completion of Stage I and the complete formal oxidation to Fe^{4+} . The Li_2O -peaks are seen to be strengthened in the second half of this charge step, further suggesting finalisation of the initial conversion. As the same cut-off potential is used for the second charge, this also shows that the potential for extraction of the remaining Li^+ is lowered after the initial extraction. During the second charge, a total of 1 Li^+ is extracted, making the total number of Li^+ extracted from the pristine state 2.3. The additional capacity is not fully recoverable during the second discharge, but the capacity from the first plateau is doubled, while the second plateau remains the same, for a total reinsertion of 0.6 Li^+ .

At this point, the centroid position of the pre-edge feature has shifted to a value very similar to the fully charged state after reaching completion of Stage II-charging, corresponding to an average oxidation state of $\text{Fe}^{3.5+}$. This could indicate a situation where not all the material is available for reinsertion, perhaps due to morphological changes caused by the reconstruction during Stage I. It is then conceivable that initially only about half of the material can facilitate the insertion of one Li^+ with a corresponding reduction of $\text{Fe}^{4+} \rightarrow \text{Fe}^{3+}$, in a reversible reaction that could be described as:



in which the additional Li^+ must occupy tetrahedral voids, although this reaction remains speculative.

The idea that some of the particles are left inactive after the initial reconstruction is supported by the evolution of discharge capacity as shown in coin cell experiments (Figure 2, left panel). The observed increase in capacity with additional cycles then indicates that more and more of the material becomes available for cycling. The elongation of the first plateau noted above is seen in coin cells as well (Figure S26), and by the 10th discharge cycle, the length of the plateau has more than doubled. At the same time, the potential of the second plateau increases from 2.0 to 2.5 V, while the potential of the charging process is lowered, overall reducing the overpotential significantly (Figure S29).

Stage II-Termination | LFO

Upon further charging of LFO into Stage II, there is a long plateau corresponding to the extraction of about one electron where there are only small variations in the pre-edge position. This indicates further extraction of Li^+ with all oxidation attributable to another species than Fe^{4+} . In this region, Zhan et al. showed the onset of increased oxygen outgassing. Hence, we propose that the charging proceeds according to a reaction that yields a deficient rocksalt phase:



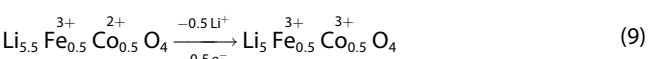
For the extraction of approximately one more electron, the Fe pre-edge peak shifts slightly towards lower energies. Such a reduction has been observed previously, and ascribed to reduction of Fe back to Fe^{3+} .^[27] However, this is not consistent with our findings. The pre-edge feature centroid position shifts back only a little less than halfway (~0.3 eV) above the pristine state, indicating an average oxidation state closer to $\text{Fe}^{3.5+}$ at the end of Stage II. This implies a total oxidation corresponding to 1.5 electrons, that is assumed to come from further outgassing of oxygen. There is no indication of change in local coordination for Fe, neither are there any signs for return of crystallinity in the diffraction patterns. We conclude that the material is either a highly disordered (and strained) rocksalt

phase or becomes X-ray amorphous owing to being nanocrystalline. Upon discharge after the initial extraction of 4 Li^+ , there is a reversible insertion of just 1 Li^+ . This occurs along with a continuous reduction of Fe, where Fe is actually reduced beyond Fe^{3+} . This process is almost entirely reversible, as upon recharging, the full capacity is almost retained, and the Fe pre-edge shifts back to the same energy as after the first charge. The second discharge cycle shows a somewhat lower discharge capacity, but this capacity loss could possibly be attributed to a higher current density used at the end of the second charge cycle of 100 mA g^{-1} , visible as a jump in potential towards the end of the second charge cycle (Figure 8). Both the potential profile and cyclic voltammogram (Figure S28, top right) resembles what has previously been reported for various electroactive polymorphs of LiFeO_2 ,^[56–58] where some authors presented evidence from XANES that the $\text{Fe}^{2+}/\text{Fe}^{3+}$ redox couple was involved in the electrochemical activity^[59] as was seen above for LFO. It is likely that the resulting material following Stage II-termination is closely related.

2.3.3. $\text{Li}_{5.5}\text{Fe}_{0.5}\text{Co}_{0.5}\text{O}_4$

Stage I-Termination | LFCO

During Stage I in LFCO, there is an initial sharp increase in the Co pre-edge position by 0.8 eV for the removal of the first 0.5 Li^+ , while the Fe pre-edge position is barely changed (Figure 10, left panel). This is in line with expectations from electronic structure calculations, which show Co 3d-states at the Fermi-level for LFCO, above the Fe 3d-states.^[45] The change in the Co pre-edge peak position at this point is approximately half of what is observed for LCO, and suggests that the initial reaction corresponds to an exclusive oxidation of $\text{Co}^{2+} \rightarrow \text{Co}^{3+}$. This would suggest an initial reaction step that can be described as:



This oxidation initially happens concurrently with a slight shift in the Bragg peak positions for the antifluorite phase towards higher Q (Figure 11, left panels), meaning a lowering in lattice parameters. This indicates an initial topotactic reaction, which is uniquely observed for LFCO among the materials under study in this work. However, the shift in peak positions does not occur for the entire initial oxidation process, and the peaks rapidly stop shifting and instead starts decreasing in intensity, similarly to what is observed for both LFO and LCO. The XANES-spectra also suggest an immediate onset of the transition from $T_d \rightarrow O_h$ symmetry for both Co and Fe (Figure 4). The same flat potential plateau is observed for LFCO as well, indicating that the entire Stage I process should be considered a two-phase reaction.

The reaction continues for the removal of one additional Li^+ , where a concurrent oxidation of Co and Fe is observed. The Co pre-edge position does not shift as rapidly in this process, and it reaches about 1.2 eV above the pristine state, while the

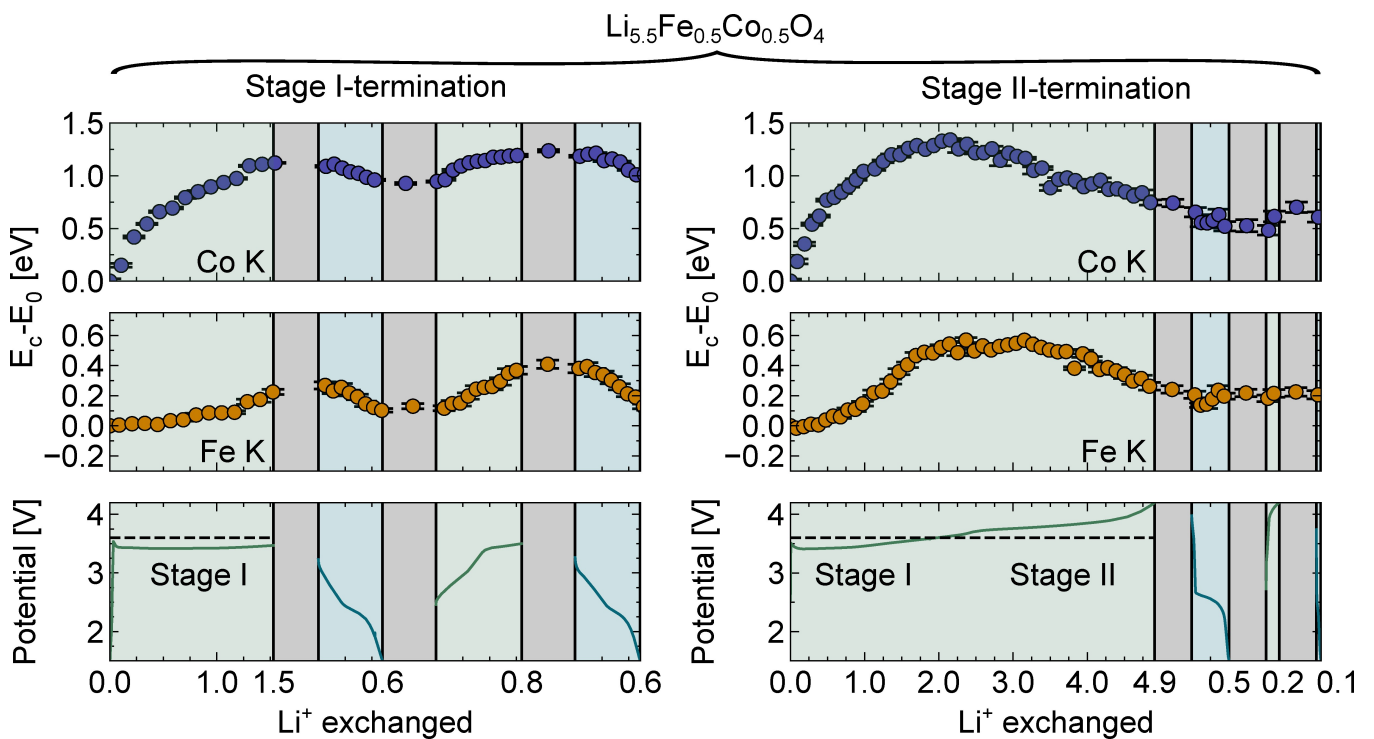


Figure 10. Combined galvanostatic cycling (potential vs. Li/Li^+) and relative position of the XANES Fe and Co K pre-edge peaks as a function of Li^+ exchanged in $\text{Li}_{5.5}\text{Fe}_{0.5}\text{Co}_{0.5}\text{O}_4$ following (Left panels) Stage I-termination and subsequent cycling and (Right panels) Stage II-termination and subsequent cycling. Note that Stage I is constructed from data from two different cells, merged between end of the first charge and start of first discharge. Charge (green) and discharge steps (blue) are separated by a resting step (gray) of 15 minutes to ensure collection of XANES-spectra while resting. Position of the pre-edge peak is given relative to the initial value before cycling. Counting of exchanged Li^+ is reset after each resting step, where the zero labels have been omitted for legibility.

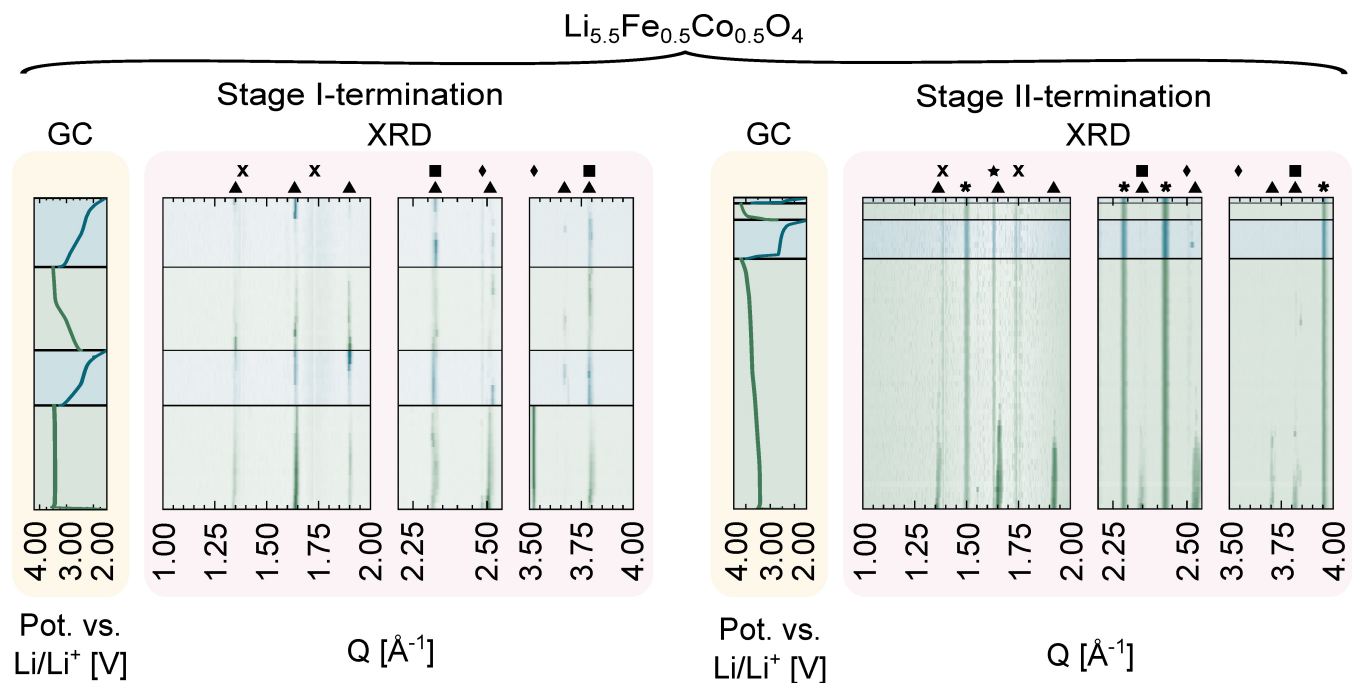


Figure 11. Operando X-ray diffractograms (XRD) of selected values of Q for LF CO and corresponding potential curves (GC) during (Left panels) Stage I-termination and subsequent cycling and (Right panels) Stage II-termination and subsequent cycling. Note that Stage I is constructed from data from two different cells, merged between end of the first charge and start of first discharge. Runs from bottom to top, with charge steps in green and discharge steps in blue. Intensities plotted as $\log I$ for enhanced contrast. Symbols above indicate peak positions of LF CO (▲), Li_2O (■), Li_2O_2 (*), Li_2CO_3 (★) and the Li-metal negative electrode (◆). Artefacts following background subtraction are also marked (x). Full diffractograms given in Figures S19 and S20.

Fe pre-edge reaches 0.3 eV above the pristine state. Note that for Stage I (Figure 10, left), the cut-off voltage was lowered by 0.1 V with respect to the half-way point, and the Co and Fe pre-edges are observed to shift further to 1.3 eV and 0.5 eV above the pristine state at the midway point during Stage II (Figure 10, right), respectively. For Fe, this corresponds to the same magnitude as the $\text{Fe}^{3+} \rightarrow \text{Fe}^{4+}$ process for LFO, while for Co, this is closer to an average oxidation state of $\text{Co}^{3.5+}$. This means that the Fe- and Co-containing product would require an additional charge compensation of 0.75 electrons, which would likely come from oxidation of oxide ions and subsequent O_2 -outgassing. The changes in the pre-edge peak positions for both Fe and Co are seen to flatten out when nearing the midway point, indeed indicating that another redox process dominates towards the end of Stage I, and there are also signs of Li_2O -formation, at $Q=2.45 \text{ \AA}^{-1}$ and 3.8 \AA^{-1} , overlapping with the corresponding peaks in the β -LFCO phase (Figure 11). At the halfway point in Stage II (after extraction of 2 Li^+), the antifluorite Bragg peaks are almost completely gone. We note that they still remain at the end of Stage I due to the lowered cut-off voltage, and there are in addition still remnant signs of the characteristic shoulder peak B in the XANES-spectra that is associated with tetrahedral symmetry (Figure S1).

Upon discharge, a two-step discharge curve is observed that is very similar to that of LCO, indicating that the reconstruction process during Stage I is similar and likely also results in a rocksalt-variant that facilitates reinsertion of Li^+ in the same manner. As we make no observations of Bragg peaks associated with the same kind of layered phase that was observed for LCO, which the subsequent discharge behaviour in LCO was attributed to, we instead suggest that this is a cation-disordered phase. Due to the structural similarities between LCO and LFCO,^[45] one could expect a similar collective migration to a layered structure as described for LCO (Figure 7) and the emergence of the same (00l)-peak. However, the observed difference could stem from the different local environments surrounding each Co^{2+} (one Li^+ -vacancy) and Fe^{3+} (two Li^+ -vacancies) in the pristine state, and the initial selective oxidation of Co over Fe. Combined, this could make the same kind of collective migration electrostatically unfavourable compared to a more disordered structure, as was suggested for LFO.

Only 0.6 Li^+ is reinserted during the initial discharge, which is lower than what is observed in coin cell experiments (Figure S26), and could be attributed to the lowered cut-off voltage during *operando* experiments not allowing Stage I to reach completion during the initial charge step. The first of the two slopes goes from 3 to 2.3 V, and there is little movement in either the Fe and Co pre-edge feature position during this step, indicating that this is primarily associated with anionic redox. The same plateau is observed in the second discharge, showing that this is a reversible process, and it is likely that this proceeds in the same manner as was observed for LCO, where it was attributed to the reversible formation of Li_2O_2 from Li_2O according to Eq. (2). The Li_2O -peaks, especially the one at $Q=3.8 \text{ \AA}^{-1}$, seems to diminish in intensity during the first discharge step, and increase again towards the end of the second charge

step, which would support this hypothesis. However, as per the discussion above, no Li_2O_2 was formed during Stage I, and we note that we see no diffraction peaks associated with Li_2O_2 . One possibility is that instead of Li_2O_2 -formation, some intermediate peroxides are formed within the structure, as was suggested by Jun et al. in the case of LCO.^[33] This would account for some, if not all, of the charge balance needed in the Fe- and Co-containing product, instead of the O_2 -release assumed above. This could also, at least partially, be the case for LCO.

Towards the end of each discharge step, there is a strengthening of the Bragg peaks associated with β -LFCO, and the B-feature in the XANES-spectra associated with tetrahedrally coordinated Fe and Co gains intensity (Figure S3), indicating the return of T_d symmetry for some of the transition metal cations, although a complete reversible return to the antifluorite structure is not observed. This is possibly an effect of the small remaining fraction of the pristine state that did not complete reconstruction during the initial charge, that could facilitate the recrystallisation of the β -LFCO phase for a small fraction of the Li^+ reinserted.

The second charge step has a three-step behaviour, in which the first two are very similar to what is observed in LCO. The last step is a fairly flat plateau that coincides with the Stage I-charging potential, thus likely associated with a continuation of Stage I. This is similar to what was observed for LFO, also here showing a lowering of the potential associated with the remaining Li^+ -extraction. In this last segment, there is little activity from Co, with the pre-edge feature position flattening out at around 1.25 eV vs. the pristine state. The pre-edge feature of Fe keeps rising, and reaches a value of 0.4 eV above the pristine state. In the second discharge step, the same behaviour as in the first is observed towards the end of discharge, although less pronounced. Especially the return of the T_d -related XANES-peaks is seen to have diminished (Figure S7), which suggests that the last charge plateau indeed is related to a continuation and gradual completion of Stage I.

Stage II-Termination | LFCO

Extending the the first charge step into Stage II (Figure 8, right), the centroid position of the Fe pre-edge feature remains flat for the next two electrons following the initial $\text{Fe}^{3+} \rightarrow \text{Fe}^{4+}$ oxidation, while for Co it decreases to the value seen for Co^{3+} for LCO (0.9 eV above the pristine state), indicating a reduction of Co from an average value of $\text{Co}^{3.5+}$ to Co^{3+} in this region. This requires that a total of 2.25 electrons need to come from an oxidation process involving neither Fe nor Co to compensate for both Li^+ extraction and reduction of Co.

No signs of any remaining or remerging crystallinity is observed (Figure 11), although it is noted that like LFO, a disordered rocksalt variant would have overlapping peaks with the aluminium current collector, potentially masking any emergent peaks. Similar persistent Li_2O_2 -peaks as seen in the diffractograms for LCO are visible, but with a much higher intensity, as well as peaks associated with Li_2CO_3 . These are all seen to be present from the start of the experiment, and

remains constant throughout the entire process with no discernible change in intensities, and is thus assumed to be impurities on the Li-metal negative electrode disk that do not partake in any reactions.

On further extraction of the last Li^+ , both Fe and Co are reduced. The Fe pre-edge shifts to a value 0.25 eV above the pristine state, indicating a mixture of $\text{Fe}^{3+}/\text{Fe}^{4+}$. The Co pre-edge shifts to a value of 0.75 eV, which indicates a mixture of $\text{Co}^{2+}/\text{Co}^{3+}$, skewed towards Co^{3+} . This mixing makes it difficult to quantify, but assuming that the energy shift of the pre-edge feature is strictly linear between each valence state, linear interpolation would yield average oxidation states of approximately $\text{Fe}^{3.5+}$ and $\text{Co}^{2.833+}$, requiring an additional 1/3 electrons from O_2 -formation, for a total of 4/3 electrons per formula unit for the last Li^+ .

As with LCO, there is a short plateau of 0.5 Li^+ in the first discharge cycle following Stage II-termination, which is associated with a slight reduction in Co. The Co pre-edge feature returns to the same value as at the end of Stage II in the subsequent charge step, although the charge capacity is significantly lower (0.2 Li^+) indicating that most of the discharge capacity is not charge compensated by the reduction of Co. The oxidation state of Fe remains constant throughout all subsequent charge and discharge steps, in stark contrast to the behaviour in LFO. There is almost no discharge capacity in the second discharge, leaving the material almost completely inactive after the first two cycles, in line with what is observed in coin cell experiments (Figure 2).

3. Conclusions

Li_5FeO_4 (LFO), Li_6CoO_4 (LCO) and the intermediate $\text{Li}_{5.5}\text{Fe}_{0.5}\text{Co}_{0.5}\text{O}_4$ (LFCO) were investigated as positive electrode materials for Li-ion batteries in combined *operando* XANES- and XRD-experiments. All materials exhibit the same kind of two-step behaviour during initial charge (Stages I and II), and subsequent electrochemical activity was investigated following an initial charge cycle that was terminated after Stage I or Stage II. By tracking the energy shifts of the pre-edge feature present in both Fe and Co K-edges, a visual representation was presented of the relative participation of Fe and Co in the charge compensation, as well as indirect evidence for participation of anionic redox, at various stages of cycling. For LCO, it was shown that after an initial cationic oxidation of Co^{2+} to Co^{4+} , an anionic redox contribution was observed for the extraction of 0.4 Li^+ , that is linked to the formation and partial oxidation of Li_2O to Li_2O_2 , alongside the formation of a Li-rich layered phase Li_2CoO_3 . This process was seen to be reversible in tandem with the $\text{Co}^{3+}/\text{Co}^{4+}$ redox couple following a Stage I-termination for at least the next two cycles during *operando* experiments, and even further in coin cell experiments, before quickly diminishing. Similar signs of reversible anionic redox contribution is seen in LFCO, although in this case Co never reaches a higher average oxidation state than $\text{Co}^{3.5+}$, and there are instead signs that peroxide species at least partially form within the structure rather than from Li_2O . In addition, the

structural changes that occur during Stage I is found to differ between them, despite the structural similarities of pristine LCO and LFCO: LFCO does not form a layered product after Stage I. These differences could be the origin of the relatively higher cycle life of LFCO observed in coin cell experiments. In LFO, a process that leads to the decomposition of LFO into cation-disordered Li_2FeO_3 , Li_2O and some O_2 -outgassing is proposed to account for the electrochemical activity during Stage I, challenging previous pictures of this initial mechanism.

Stage II-termination resulted in a rapidly diminishing capacity for LCO and LFCO, rendering the materials almost completely inactive after the initial charging. While this rules them out for use as electrode materials under these conditions, it instead makes them suitable as sacrificial additives to other electrode materials that can compensate for the high first-cycle loss of active Li^+ certain negative electrode materials exhibit. LFO on the other hand showed a much higher reversible capacity following Stage II-termination than LFCO and LCO over up to 400 cycles in a half-cell configuration, albeit following a different mechanism than what followed from Stage I-termination of LFO, resembling the cycle profile of electrochemically active polymorphs of LiFeO_2 . Further cycling appears to involve both Fe^{2+} , Fe^{3+} and Fe^{4+} . It is shown upon charging into Stage II for all materials that neither Fe nor Co is oxidised beyond the oxidation states reached in Stage I (Co^{4+} in LCO, Fe^{4+} in LFO and $\text{Fe}^{4+}/\text{Co}^{3.5+}$ in LFCO), and instead is reduced during further Li^+ extraction, suggesting that Stage II-charging is associated considerable decomposition with much irreversible loss of oxygen.

This work has also shown that tracking the energy shifts of the pre-edge position is an effective way to visually correlate redox activity in Fe- and Co-based materials to galvanostatic cycling data to aid in elucidating the underlying reaction mechanisms.

Experimental

Materials Synthesis

Powder samples of Li_5FeO_4 , $\text{Li}_{5.5}\text{Fe}_{0.5}\text{Co}_{0.5}\text{O}_4$ and Li_6CoO_4 were synthesised from stoichiometric mixtures of Li_2O (Sigma-Aldrich, 97%): Fe_2O_3 (Acros Organics, 99.999% trace metal basis):CoO (Acros Organics, >99%) through a solid-state reaction pathway. As Li_2O readily reacts with moisture in the atmosphere to form LiOH , the reactant powder was first subjected to heat treatment at 500 °C for 12 h under an Ar-flow of 100 ml/min in a semiclosed system to decompose and remove LiOH prior to mixing. Since both Li_2O and the products readily reacts with moisture and CO_2 in ambient air, all processing steps were done in an Ar-filled glovebox. The precursors were manually ground for 20 minutes. The solid state reactions were done in a split furnace where the mixed precursors were placed in an alumina boat inside a quartz tube capped at both ends with adaptors to keep the system closed. These adaptors could then be connected to either an Ar-flow or a vacuum pump, and at the end of the synthesis transferred back to the glovebox for further handling. Li_5FeO_4 was synthesised in a semi-closed setup under an Ar-flow of 100 ml/min for 20 h, while Li_6CoO_4 and $\text{Li}_{5.5}\text{Fe}_{0.5}\text{Co}_{0.5}\text{O}_4$ were synthesised under active vacuum in order to prevent any oxidation of Co^{2+} to Co^{3+} from trace amounts of

oxygen in the Ar-gas. All products were further hand-ground in an agate mortar prior to electrode preparation and electrochemical testing.

Electrode Preparation

Due to the moisture sensitivity of the active materials, all electrodes were prepared inside an Ar-filled glovebox. Slurries were made in a 70:20:10 mixture (wt%) of active material, binder (PVDF, Arkema Kynar HSV1810) and conductive additive (Super P, TIMCAL/Imerys), and dissolved in NMP (Sigma-Aldrich). The slurry was thoroughly mixed in a Thinky ARE-250 mixer, and subsequently coated on a carbon coated aluminium foil (Cambridge Energy Solutions) inside the glovebox. The electrodes were left to dry inside the glovebox overnight, and any residual NMP were dried in a Büchi oven under vacuum for up to five hours the following day. All electrodes were kept in sealed bags inside a glovebox until use, and individual electrode disks were cut out with a cathode cutter from Hohsen.

Coin Cell Electrochemical Testing

All coin cells were assembled and tested in half-cell configuration in CR2032 stainless steel (SS304) cases from PI-KEM. The cells were assembled inside the glovebox, and consisted of a lithium metal disk (Sigma-Aldrich), a glass fibre separator (Whatman), electrode disks prepared as described above, a stainless steel spacer and washer. Commercial LP30 (Sigma-Aldrich) was used as electrolyte. All galvanostatic measurements were done with a specific current of 100 mA g^{-1} , within voltage windows specified in the text. The cut-off voltages were raised for the first part of the formation charge cycles to avoid premature termination due to the presence of an initial potential barrier. For all galvanostatic measurements, a BTS4000 cycler (Neware) was used. Cyclic voltammetric measurements were done following an initial galvanostatic formation step (Stage I and Stage II) with a scanning rate of 0.1 mV s^{-1} on a MPG-2 cycler (BioLogic).

Operando Electrochemical Testing

Operando experiments were carried out at the Swiss-Norwegian Beamlines (SNBL, BM31) at the European Synchrotron Radiation Facility (ESRF) in Grenoble, France. Cells were assembled in an Ar-filled glovebox in custom *operando* cells based on the design by Drozhzhin et al.^[60] Electrodes were pre-cut inside the glovebox in the home lab, sealed and transported to ESRF for assembly on-site. The cells were cycled with a portable BAT-SMALL cycler (Astrol Electronic AG). The cells were mounted in a sample holder mounted on a programmable xy-stage that allowed movement of the sample holder between pre-calibrated positions. Up to six *operando* cells were cycled at once, and XANES- and XRD-data were collected for each sample before moving to the next. Cells for Stage I were cycled at 75 mA g^{-1} for the initial charging step, and 50 mA g^{-1} for subsequent cycles. Cells for Stage II were cycled at 50 mA g^{-1} for the initial charging step, and 35 mA g^{-1} for subsequent cycles. Data for LFCO Stage I consists of two different cells, both cycled at the same specific current as specified above, but where the cut-off voltage was reduced from 3.6 V to 3.5 V in the second cell. Data from the first cell is included up until 3.5 V. The cell for LFO Stage II had its specific current increased from 35 mA g^{-1} to 100 mA g^{-1} towards the end of the second charge step.

X-Ray Absorption Near-Edge Spectroscopy (XANES)

The XANES-data was measured in transmission mode at SNBL, BM31. Spectra of Fe- and Co-metal foils were captured before sample measurements, and were used to calibrate the energy against tabulated values in International Tables for Crystallography Vol. C.^[61] Linear functions were fitted to the pre-edge and post-edge areas, where the pre-edge function was subtracted from the data. Each spectrum was later normalised by dividing by the difference between the pre-edge and post-edge fitted functions at the estimated edge position. The centroid position of the pre-edge feature was taken as the mean value (μ) of a Pseudo-Voigt peak function fitted to the pre-edge peak following background subtraction of the rising edge contribution. The rising edge background was fitted with an arctangent function. All curve fits were done using a non-linear least squares method as implemented in SciPy.^[62]

X-ray Diffraction (XRD)

Synchrotron radiation X-ray diffraction data were collected at SNBL, BM31. The diffraction patterns were collected with a Dexela 2D-detector using a wavelength of 0.3396 \AA . A total of 15 diffractograms were captured per measurement, each constituting a 1 s exposure, and were subsequently averaged. For every five diffractograms, another five darks were measured, averaged and subtracted from the preceding diffractograms to remove background noise. The 2D-data was integrated using the azimuthal integrator implemented in pyFAI.^[63] A LaB_6 -standard (NIST Standard Reference Material 660c) were measured in each sample holder position to refine experimental geometry parameters used for integration. All diffraction patterns are reported in Q , with the relation to the wavelength of the radiation (λ) and the scattering angle (θ) given by $Q = \frac{4\pi}{\lambda} \sin\theta$.

Acknowledgements

The authors gratefully express thanks for being granted synchrotron beamtime at SNBL (ESRF) and for the skillful assistance provided by the SNBL staff prior to, during and after the experiments. In particular we would like to thank Kenneth Marshall, Dragos Stoian, Vadim Dyadkin and Wouter van Beek. HHH acknowledges funding through MoZEEs, a Norwegian Centre for Environment-friendly Energy Research (FME), co-sponsored by the Research Council of Norway (project number 257653) and 40 partners from research, industry, and public sector.

Conflict of Interests

The authors declare no conflict of interest.

Data Availability Statement

The data that support the findings of this study are available from the corresponding author upon reasonable request.

Keywords: electrochemistry • anionic redox • Li-rich • Li-ion batteries

- [1] S. Fankhauser, S. M. Smith, M. Allen, K. Axelsson, T. Hale, C. Hepburn, J. M. Kendall, R. Khosla, J. Lezaun, E. Mitchell-Larson, M. Obersteiner, L. Rajamani, R. Rickaby, N. Seddon, T. Wetzer, *Nat. Clim. Change* **2022**, *12*, 15–21.
- [2] H. Van Coppenolle, M. Blondeel, T. Van De Graaf, *Global Policy* **2023**, *14*, 48–60.
- [3] *World Energy Outlook 2023*, International Energy Agency (IEA), Paris, 2023.
- [4] C. Wu, X.-P. Zhang, M. J. H. Sterling, *IEEE Access* **2021**, *9*, 113169–113186.
- [5] H. Zsiborács, G. Pintér, A. Vincze, Z. Birkner, N. H. Baranyai, *Energy Reports* **2021**, *7*, 3805–3818.
- [6] D. Solyali, B. Safaei, O. Zargar, G. Aytac, *Int. J. Energy Res.* **2022**, *46*, 17786–17812.
- [7] *Global EV Outlook 2023*, International Energy Agency (IEA), Paris, 2023.
- [8] A. Manthiram, *Nat. Commun.* **2020**, *11*, 1550.
- [9] W. Li, E. M. Erickson, A. Manthiram, *Nat. Energy* **2020**, *5*, 26–34.
- [10] X.-G. Yang, T. Liu, C.-Y. Wang, *Nat. Energy* **2021**, *6*, 176–185.
- [11] C. P. Grey, D. S. Hall, *Nat. Commun.* **2020**, *11*, 6279.
- [12] J. Xu, X. Cai, S. Cai, Y. Shao, C. Hu, S. Lu, S. Ding, *Energy Environ. Mater.* **2023**, *6*, e12450.
- [13] G. Assat, J. M. Tarascon, *Nat. Energy* **2018**, *3*, 373–386.
- [14] M. Zhang, D. A. Kitchaev, Z. Lebans-Higgins, J. Vinckeviciute, M. Zuba, P. J. Reeves, C. P. Grey, M. S. Whittingham, L. F. J. Piper, A. Van Der Ven, Y. S. Meng, *Nat. Rev. Mater.* **2022**, *7*, 522–540.
- [15] A. D. Robertson, P. G. Bruce, *Chem. Mater.* **2003**, *15*, 1984–1992.
- [16] D. Y. W. Yu, K. Yanagida, Y. Kato, H. Nakamura, *J. Electrochem. Soc.* **2009**, *156*, A417.
- [17] M. Sathiya, G. Rousse, K. Ramesha, C. P. Laisa, H. Vezin, M. T. Sougrati, M. L. Doublet, D. Foix, D. Gonbeau, W. Walker, A. S. Prakash, M. Ben Hassine, L. Dupont, J. M. Tarascon, *Nat. Mater.* **2013**, *12*, 827–835.
- [18] M. Sathiya, K. Ramesha, G. Rousse, D. Foix, Gonbeau, A. S. Prakash, M. L. Doublet, K. Hemalatha and J.-M. Tarascon, *Chem. Mater.* **2013**, *25*, 1121–1131.
- [19] N. Yabuuchi, M. Takeuchi, M. Nakayama, H. Shiiba, M. Ogawa, K. Nakayama, T. Ohta, D. Endo, T. Ozaki, T. Inamasu, K. Sato, S. Komaba, *Proc. Natl. Acad. Sci. USA* **2015**, *112*, 7650–7655.
- [20] Y. Y. Hwang, J. H. Han, S. H. Park, J. E. Jung, N. K. Lee, Y. J. Lee, *Nanotechnology* **2022**, *33*, 182003.
- [21] G. Demoisson, F. Jeannot, C. Gleitzer, J. Aubry, *C. R. Acad. Sc. Paris* **1971**, *272*, 458–461.
- [22] S. Narukawa, Y. Takeda, M. Nishijima, N. Imanishi, O. Yamamoto, M. Tabuchi, *Solid State Ionics* **1999**, *122*, 59–64.
- [23] A. Hirano, T. Matsumura, M. Ueda, N. Imanishi, Y. Takeda, M. Tabuchi, *Solid State Ionics* **2005**, *176*, 2777–2782.
- [24] N. Imanishi, Y. Inoue, A. Hirano, M. Ueda, Y. Takeda, H. Sakaebe, M. Tabuchi, *J. Power Sources* **2005**, *146*, 21–26.
- [25] C. S. Johnson, S. H. Kang, J. T. Vaughey, S. V. Pol, M. Balasubramanian, M. M. Thackeray, *Chem. Mater.* **2010**, *22*, 1263–1270.
- [26] T. Okumura, M. Shikano, H. Kobayashi, *J. Mater. Chem. A* **2014**, *2*, 11847–11856.
- [27] C. Zhan, Z. Yao, J. Lu, L. Ma, V. A. Maroni, L. Li, E. Lee, E. E. Alp, T. Wu, J. Wen, Y. Ren, C. Johnson, M. M. Thackeray, M. K. Chan, C. Wolverton, K. Amine, *Nat. Energy* **2017**, *2*, 963–971.
- [28] L. Li, E. Lee, J. W. Freeland, T. T. Fister, M. M. Thackeray, M. K. Chan, *J. Phys. Chem. Lett.* **2019**, *10*, 806–812.
- [29] H. Kobayashi, Y. Nakamura, M. Nakayama, S. Kodaki, R. Matsuo, I. Honma, *Adv. Energy Mater.* **2023**, *13*, 2203441.
- [30] R. Luge, R. Hoppe, Z. Anorg. Allg. Chem. **1986**, *534*, 61–68.
- [31] Z. Chen, Z. Zhang, J. Li, *Phys. Chem. Chem. Phys.* **2018**, *20*, 20363–20370.
- [32] H. Kobayashi, T. Tsukasaki, Y. Ogasawara, M. Hibino, T. Kudo, N. Mizuno, I. Honma, K. Yamaguchi, *ACS Appl. Mater. Interfaces* **2020**, *12*, 43605–43613.
- [33] K. Jun, L. Kaufman, W. Jung, B. Park, C. Jo, T. Yoo, D. Lee, B. Lee, B. D. McCloskey, H. Kim, G. Ceder, *Adv. Energy Mater.* **2023**, *13*, 2301132.
- [34] W. Lee, H. Lee, Y. Byeon, J. H. Kim, W. Choi, M. Choi, M.-S. Park, W.-S. Yoon, *Adv. Energy Mater.* **2023**, *13*, 2302316.
- [35] Z. Yao, M. K. Chan, C. Wolverton, *Chem. Mater.* **2022**, 4536–4547.
- [36] Y. G. Lim, D. Kim, J. M. Lim, J. S. Kim, J. S. Yu, Y. J. Kim, D. Byun, M. Cho, K. Cho, M. S. Park, *J. Mater. Chem. A* **2015**, *3*, 12377–12385.
- [37] M. Noh, J. Cho, *J. Electrochem. Soc.* **2012**, *159*, A1329–A1334.
- [38] X. Su, C. Lin, X. Wang, V. A. Maroni, Y. Ren, C. S. Johnson, W. Lu, *J. Power Sources* **2016**, *324*, 150–157.
- [39] L. Zhang, W. M. Dose, A. D. Vu, C. S. Johnson, W. Lu, *J. Power Sources* **2018**, *400*, 549–555.
- [40] W. M. Dose, C. Villa, X. Hu, A. R. Dunlop, M. J. Piernas-Muñoz, V. A. Maroni, S. E. Trask, I. Bloom, V. Dravid, C. S. Johnson, *J. Electrochem. Soc.* **2020**, *167*, 160543.
- [41] M.-S. Park, Y.-G. Lim, S. M. Hwang, J. H. Kim, J.-S. Kim, S. X. Dou, J. Cho, Y.-J. Kim, *ChemSusChem* **2014**, *7*, 3138–3144.
- [42] Y. Guo, X. Li, Z. Wang, H. Guo, J. Wang, *J. Energy Chem.* **2020**, *47*, 38–45.
- [43] F. Stewner, R. Hoppe, *Acta Crystallogr. Sect. B* **1971**, *27*, 616–621.
- [44] R. Hoppe, H. König, Z. Anorg. Allg. Chem. **1977**, *430*, 211–217.
- [45] R. V. Thøgersen, A. S. Fjellvåg, Ø. S. Fjellvåg, H. Fjellvåg, Z. Anorg. Allg. Chem. **2023**, *649*, e202300146.
- [46] J. Li, B. Zhu, S. Li, D. Wang, W. Zhang, Y. Xie, J. Fang, B. Hong, Y. Lai, Z. Zhang, *J. Electrochem. Soc.* **2021**, *168*, 080510.
- [47] T. Yamamoto, *X-Ray Spectrom.* **2008**, *37*, 572–584.
- [48] G. S. Henderson, F. M. de Groot, B. J. Moulton, *Spectrosc. Methods Mineral. Mater. Sci.* **2014**, *78*, 75–138.
- [49] M. Wilke, F. Farges, P. E. Petit, G. E. Brown, F. Martin, *Am. Mineral.* **2001**, *86*, 714–730.
- [50] M. Vračar, A. Kuzmin, R. Merkle, J. Purans, E. A. Kotomin, J. Maier, O. Mathon, *Phys. Rev. B* **2007**, *76*, 174107.
- [51] J. Blasco, B. Aznar, J. García, G. Subías, J. Herrero-Martín, J. Stankiewicz, *Phys. Rev. B* **2008**, *77*, 054107.
- [52] A. E. Bocquet, A. Fujimori, T. Mizokawa, T. Saitoh, H. Namatame, S. Suga, N. Kimizuka, Y. Takeda, M. Takano, *Phys. Rev. B* **1992**, *45*, 1561–1570.
- [53] M. Abbate, G. Zampieri, J. Okamoto, A. Fujimori, S. Kawasaki, M. Takano, *Phys. Rev. B* **2002**, *65*, 165120.
- [54] R. V. Thøgersen, F. Bianchini, H. Fjellvåg, P. Vajeeston, *RSC Adv.* **2022**, *12*, 17410–17421.
- [55] C. Didier, W. K. Pang, Z. Guo, S. Schmid, V. K. Peterson, *Chem. Mater.* **2020**, *32*, 2518–2531.
- [56] R. Kanno, T. Shirane, Y. Kawamoto, Y. Takeda, M. Takano, M. Ohashi, Y. Yamaguchi, *J. Electrochem. Soc.* **1996**, *143*, 2435–2442.
- [57] Y. Lee, S. Sato, Y. Sun, K. Kobayakawa, Y. Sato, *J. Power Sources* **2003**, *119–121*, 285–289.
- [58] A. Abdel-Ghany, A. Mauger, H. Grout, K. Zaghib, C. Julien, *J. Power Sources* **2012**, *197*, 285–291.
- [59] S.-H. Wu, H.-Y. Liu, *J. Power Sources* **2007**, *174*, 789–794.
- [60] O. A. Drozhzhin, I. V. Tereshchenko, H. Emerich, E. V. Antipov, A. M. Abakumov, D. Chernyshov, *J. Synchrotron Radiat.* **2018**, *25*, 468–472.
- [61] *International Tables for Crystallography, Volume C*, ed. A. J. C. Wilson, Kluwer Academic Publishers, Dordrecht/Boston/London, 1992.
- [62] P. Virtanen, R. Gommers, T. E. Oliphant, M. Haberland, T. Reddy, D. Cournapeau, E. Burovski, P. Peterson, W. Weckesser, J. Bright, S. J. van der Walt, M. Brett, J. Wilson, K. J. Millman, N. Mayorov, A. R. Nelson, E. Jones, R. Kern, E. Larson, C. J. Carey, İ. Polat, Y. Feng, E. W. Moore, J. Vander-Plas, D. Laxalde, J. Perktold, R. Cimrman, I. Henriksen, E. A. Quintero, C. R. Harris, A. M. Archibald, A. H. Ribeiro, F. Pedregosa, P. van Mulbregt, A. Vijaykumar, A. P. Bardelli, A. Rothberg, A. Hilboll, A. Kloeckner, A. Scopatz, A. Lee, A. Rokem, C. N. Woods, C. Fulton, C. Masson, C. Häggström, C. Fitzgerald, D. A. Nicholson, D. R. Hagen, D. V. Pasechnik, E. Olivetti, E. Martin, E. Wieser, F. Silva, F. Lenders, F. Wilhelm, G. Young, G. A. Price, G. L. Ingold, G. E. Allen, G. R. Lee, H. Audren, I. Probst, J. P. Dietrich, J. Silterra, J. T. Webber, J. Slavić, J. Nothman, J. Buchner, J. Kulick, J. L. Schönberger, J. V. de Miranda Cardoso, J. Reimer, J. Harrington, J. L. C. Rodríguez, J. Nunez-Iglesias, J. Kuczyński, K. Tritz, M. Thoma, M. Newville, M. Kümmeler, M. Bolingbroke, M. Tartre, M. Pak, N. J. Smith, N. Nowaczyk, N. Shebanov, O. Pavlyk, P. A. Brodtkor, P. Lee, R. T. McGibbon, R. Feldbauer, S. Lewis, S. Tygier, S. Sievert, S. Vigna, S. Peterson, S. More, T. Pudlik, T. Oshima, T. J. Pingel, T. P. Robitaille, T. Spura, T. R. Jones, T. Cera, T. Leslie, T. Zito, T. Krauss, U. Upadhyay, Y. O. Halchenko, Y. Vázquez-Baeza, *Nat. Methods* **2020**, *17*, 261–272.
- [63] J. Kieffer, V. Valls, N. Blanc, C. Hennig, *J. Synchrotron Radiat.* **2020**, *27*, 558–566.

Manuscript received: June 6, 2024
Accepted manuscript online: June 20, 2024
Version of record online: August 15, 2024